Ore Geology Reviews 53 (2013) 403–421

Contents lists available at SciVerse ScienceDirect

Ore Geology Reviews

journal homepage: www.elsevier.com/locate/oregeorev

Hydrothermal alteration associated with Mesozoic granite-hosted gold mineralization at the Sanshandao deposit, Jiaodong Gold Province, China

Xiao-Chun Li [a], Hong-Rui Fan [a,*], M. Santosh [b], Fang-Fang Hu [a], Kui-Feng Yang [a], Ting-Guang Lan [a]

[a] Key Laboratory of Mineral Resources, Institute of Geology and Geophysics, Chinese Academy of Sciences, Beijing 100029, China
[b] China University of Geosciences (Beijing), Beijing 100083, China

ARTICLE INFO

Article history:
Received 15 July 2012
Received in revised form 31 January 2013
Accepted 31 January 2013
Available online 17 February 2013

Keywords:
Alteration geochemistry
Physicochemical condition
Fluid source
Sanshandao deposit
Jiaodong gold province

ABSTRACT

The Sanshandao gold deposit (reserves of more than 200 t Au and average grade of 3.96 g/t), located at northwestern edge of the Jiaodong Peninsula, eastern North China Craton, is one of the largest gold deposits in the Jiaodong gold province. In this deposit, disseminated- and stockwork-style ores are hosted in Mesozoic granitoids; mineralization and alteration are largely controlled by the regional Sanshandao–Cangshang fault. Host granitic rocks for the deposit display a complex paragenetic sequence of alteration and mineralization. Activities of the Sanshandao–Cangshang fault created structurally controlled permeability allowing for infiltration of hydrothermal fluids, leading to diffusive K-feldspar alteration on the two fault planes. Later, large scale diffusive sericitization symmetrically developed across the main fault, and partially overprinted the earlier K-feldspar alteration. Following the sericitization, relatively small scale silicification occurred, but now it is only retained in the hanging wall of the main fault. Subsequently, the fault gouge formed as a "barrier layer", which is impermeable for later fluids to move upward. After that, strong pyrite–sericite–quartz alteration occurred only in the footwall of the main fault, and was accompanied by gold precipitation. The last stage carbonation and quartz-carbonate veins marked the waning of gold-related hydrothermal activity. Mass-balance calculations indicate complex behaviors of different types of elements during fluid–rock interaction. Most major elements were affected by intensive mineral replacement reactions. As expected, the fluid-mobile elements, LILE and LREE, generally show moderate to high mobility. It is notable that even the commonly assumed fluid-immobile elements, such as HREE and HFSE, tend to be changed to various degrees. In addition, Y–Ho, Zr–Hf and Nb–Ta fractionations are observed in altered domains. Studies on alteration assemblages and fluid inclusions suggest that the ore-forming fluids were characterized by low salinity (≤8.4 wt.% NaCl equiv.), moderate temperature (300–400 °C), weakly acidic (pH: 3–5), and relatively reducing (log f_{O2}: ~−28) characteristics. In this type of fluids, gold was most likely transported as $Au(HS)_2^-$ complex. With alteration going on, log (a_K^+/a_H^+) of fluids generally decreased due to significant formation of secondary K-bearing minerals. In addition, there might be a decrease of f_{O2} from pre-gold alteration stage to the main gold mineralization stage, and decrease of f_{O2} was probably one of the factors controlling gold precipitation. The Sr and Nd isotopic compositions of hydrothermal minerals, combined with previous H–O and He–Ar isotopic studies, indicate that the hydrothermal fluids were mainly derived from crustal sources (e.g., degassing of felsic magmas and meteoric water), but with involvement of mantle derived components. The gold mineralization event just coincided with reactivation of the North China Craton, as marked by asthenosphere upwelling, voluminous igneous rocks, and high crustal heat flow, which may have provided sufficient heat energy and fluid input required for the formation of the gold deposits.

1. Introduction

The Jiaodong Peninsula is currently the most important gold province in China, with a total gold ore reserve of 1300 t (Li et al., 2007). It is located along the southeastern margin of the North China Craton (NCC), which is the largest and oldest (2.5–3.8 Ga) craton in China (Zhai and Santosh, 2011, and references therein). Mesozoic granitoids, occupying >50% of the northwestern part of the Jiaodong Peninsula, intrude into Precambrian basement rocks which have undergone amphibolite to granulite facies metamorphism. The majority of gold resources (>95%) are hosted by these granitoids, making the Jiaodong gold province one of the largest granitoid-hosted gold provinces presently recognized in the world (Qiu et al., 2002). Gold deposits of this district have been classified as the Linglong-type and the Jiaojia-type, both of which are essentially fault controlled (Lu and Kong, 1993). The Linglong-type mineralization is characterized by massive auriferous quartz veins hosted in subsidiary second- or third-order faults cutting

* Corresponding author. Tel.: +86 10 82998218; fax: +86 10 62010846.
E-mail address: fanhr@mail.iggcas.ac.cn (H.-R. Fan).

0169-1368/$ – see front matter © 2013 Elsevier B.V. All rights reserved.
http://dx.doi.org/10.1016/j.oregeorev.2013.01.020

Mesozoic granitoids, whereas the Jiaojia-type mineralization consists of disseminated- and stockwork-style ores located in regional faults, which are enveloped by broad alteration halos. Many papers, mostly in Chinese, have been published on the Jiaodong gold deposits and related igneous rocks (e.g. Chen et al., 1989, 2005; Fan et al., 2003, 2005; Goldfarb et al., 2007; Li and Yang, 1993; Li et al., 2004, 2006; Lu and Kong, 1993; Luo and Wu, 1987; Mao et al., 2008; Qiu et al., 2002; Wang et al., 1998; Yang and Lu, 1996; Yang and Zhou, 2001; Yang et al., 1998), mainly focusing on the geological features, age, fluid characteristics and geodynamic mechanism of the ore deposits. These investigations have shown that deposit mineralogy, hydrothermal fluid compositions, stable isotope compositions and ore-forming P–T conditions of the Jiaodong gold deposits are similar to those of typical orogenic gold deposits (Goldfarb et al., 2001; Qiu et al., 2002).

However, relatively few comprehensive studies have been published on gold-related wall rock alterations, especially for the Jiaojia-type gold deposit. Qiu et al (2002) briefly summarized the spatial zonation, petrography and geochemistry of alteration assemblages for both Linglong-type and Jiaojia-type mineralization. Ling et al (2002) studied the alteration geochemistry of the Dayingezhuang gold deposit and Jinqingding gold deposit in detail. Most other works only briefly introduced the spatial zonation, mineralogy and petrography of alteration assemblages.

The Sanshandao gold deposit is located at the northwestern edge of the Jiaodong Peninsula, and is one of the largest gold deposits (with reserves of more than 200 t Au and average grade of 3.96 g/t) in the Jiaodong gold province (personal communication with Mr. Xiannian Jin). This deposit is a typical Jiaojia-style gold occurrence. It is associated with the Sanshandao–Cangshang fault zone (Figs. 1 and 2), which also structurally controls the large Cangshang gold deposit located 4 km south of the Sanshandao deposit. Wide alteration zones are developed along the fault zone. In the past five years, several drill holes were made in this area under the "Deep Ore Exploration" programs, exposing excellent geological features and providing important specimen for investigations on hydrothermal alteration.

In this paper, we provide a comprehensive description of the alteration assemblages and veins of the Sanshandao gold deposit, documenting their paragenesis, spatial zonation, petrography, geochemistry and Sr–Nd isotopes of hydrothermal minerals. Based on the data, we (1) illustrate mobility of elements associated with the hydrothermal alteration; (2) more tightly constrain the physicochemical conditions of the ore fluid system and (3) better define the sources of hydrothermal fluids.

2. Regional geology

The North China Craton, with an Archean core of 2.5–3.8 Ga, comprises three major crustal blocks: the Eastern Block (Yanliao Block), the Ordos Block and the Yinshan Block (together defining the Western Block) (Zhao et al., 2001). The Jiaodong Peninsula occupies the easternmost edge of the Eastern Block of the NCC and is geologically divided into the southeastern Ludong terrane and the northwestern Jiaobei terrane by the Mishan fault (Fig. 1). The Ludong terrane petrotectonically belongs to the northern margin of the South China Block which records a subduction history associated with the Triassic collisional event (Zheng et al., 2009).

The Jiaobei terrane petrotectonically belongs to the southern margin of the NCC. Almost all gold deposits are hosted in the Jiaobei terrane (Zhai et al., 2004), and more than 80% of the gold reserves are concentrated in the Zhaoyuan–Laizhou gold belt (Fig. 1). The Precambrian basement in the Jiaobei terrane is principally defined by the Archean Jiaodong Group and the Paleoproterozoic Fenzishan and Jingshan Groups (e.g., Tam et al., 2011; Tang et al., 2007). Mesozoic magmatic rocks are widely exposed in the Jiaobei terrane and two

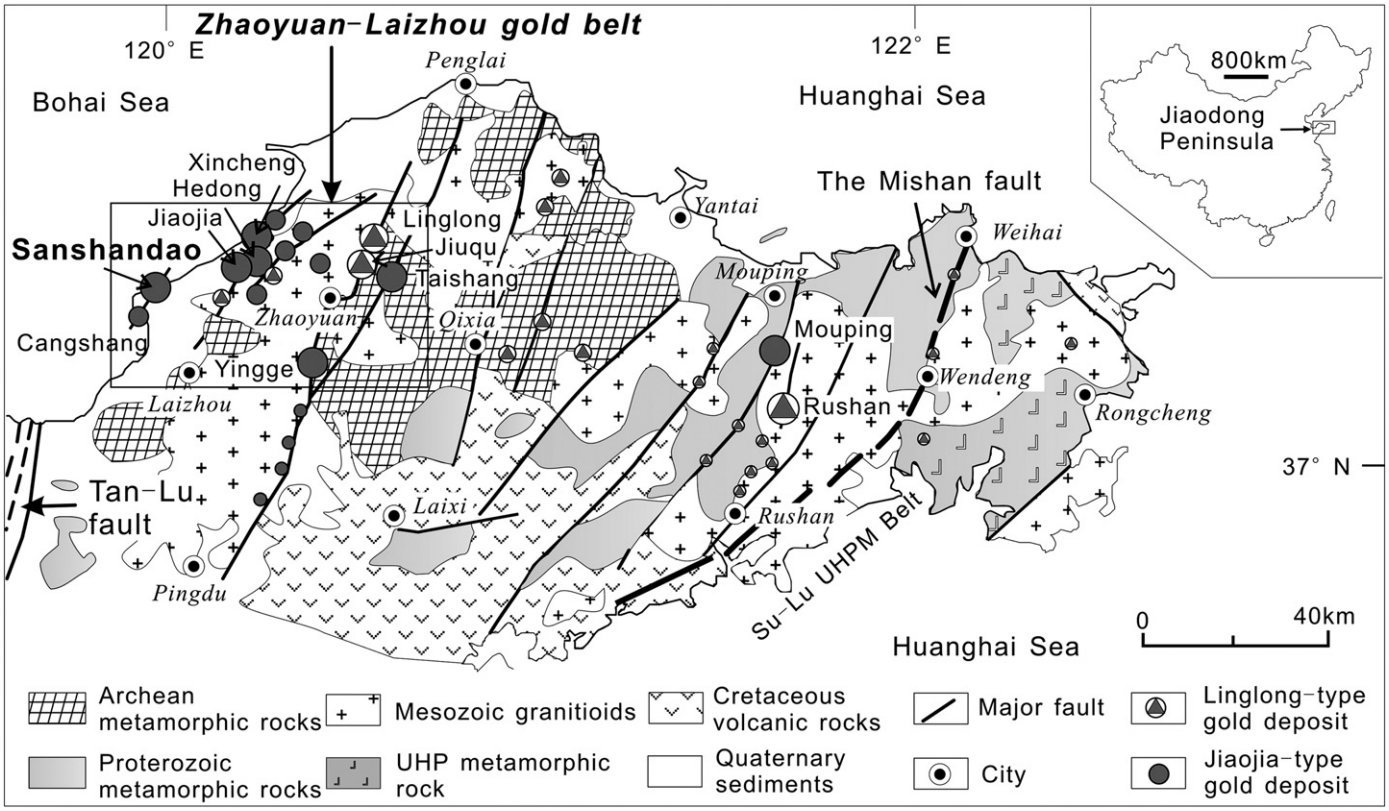

Fig. 1. Simplified geological map of the Jiaodong Peninsula showing the major tectonic units and location of the major gold deposits (after Fan et al., 2003). The size of symbols for gold deposits indicates the relative volume of gold resources: large symbol corresponds to Au >50 t, and small symbol means Au <50 t. The Sanshandao deposit occurs along the northwestern margin of the gold province.

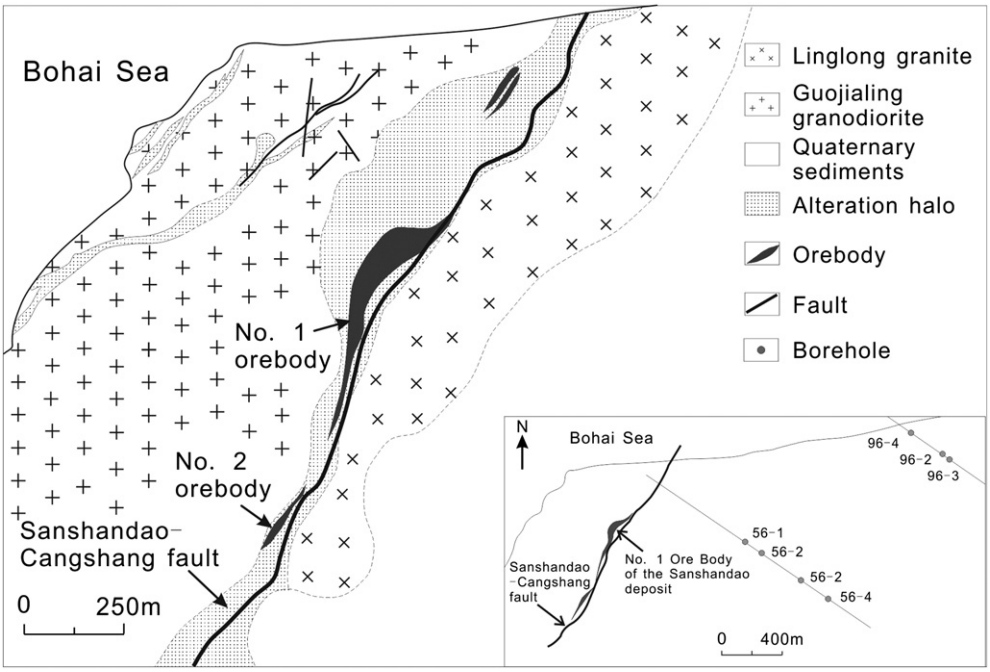

Fig. 2. Generalized geological map of the Sanshandao gold deposit (after Fan et al., 2003). Note that hydrothermal alteration halos and orebodies are controlled by the Sanshandao–Cangshang fault. The insert shows the locations of the Sanshandao deposit and studied holes.

main periods of magmatism are recognized: Jurassic and Early Cretaceous. The Jurassic magmatic activity is represented by the crustally-derived Linglong and Luanjiahe granitoids, emplaced during 158 to 160 Ma (Hou et al., 2007; Wang et al., 1998; Yang et al., 2012). In the Early Cretaceous, extensive magmatism took place through strong crust–mantle interaction, including widespread granitoids (113–130 Ma), mafic to felsic volcanic rocks in Jiaolai Basin (110–130 Ma), and numerous mafic dikes (122–124 Ma) (Fan et al., 2001; Goss et al., 2010; Li et al., 2012; Yang et al., 2004; Yang et al., 2012). The Mesozoic granitoids are potential hosts of gold deposits.

Two main phases of deformation were identified in this region during the Mesozoic. The first phase is characterized by northwest–southeast oblique compression, presumably related to the subduction of the Izanagi–Pacific plate (Wang et al., 1998), which induced prominent NNE- to NE-trending brittle-ductile shear zones with sinistral oblique reverse movements. The second phase involved the development of NNE- and NE-trending extensional brittle structures and half-graben basins, accompanied by intrusion of mafic dikes and hydrothermal gold mineralization. These structures are commonly thought to be subsidiary to the Tan–Lu fault (Yang and Lu, 1996).

3. Geology of the Sanshandao gold deposit

The Sanshandao gold deposit is located about 30 km north to the Laizhou city and occupies an area of 0.3 km^2. This deposit, first discovered in 1967 and originally developed by local prospectors for the first few years, is now being worked by the Shandong Gold Group Co. Ltd. By 2010, the known reserves were more than 200 t, the grade ranges from 3.04 to 14.56 g/t (with an average grade of 3.96 g/t), and the annual production is more than 3 t Au (personal communication with Mr. Xiannian Jin).

Four major lithological groups can be identified in the Sanshandao deposit as follows (Fig. 2): (1) Archean Jiaodong Group; (2) Jurassic Linglong granite; (3) Cretaceous Guojialing granodiorite and (4) Cretaceous mafic dikes. The Linglong granite intruded into the TTG gneiss and amphibolite of the Late Archean Jiaodong Group during 158–160 Ma. The gray granite shows a fine- to medium-grained, equigranular texture. The main mineral assemblage is plagioclase (25–30%), K-feldspar (35–40%), quartz (20–30%) and biotite (5–10%), with accessory minerals such as garnet, titanite, ilmenite, zircon and apatite. Early studies demonstrated that the Linglong granite was mainly derived from partial melting of the ancient crust in the NCC (Hou et al., 2007; Yang et al., 2012). The Guojialing granodiorite was emplaced during 126–130 Ma, and is pale red in hand specimen with porphyritic texture. The main minerals are plagioclase (35–55%), K-feldspar (10–25%), quartz (15–30%), biotite (4–6%). Titanite is the main accessory mineral, with subordinate magnetite, zircon, apatite and monazite. K-feldspar appears mainly as euhedral phenocryst, with the largest crystal measuring up to 10 cm in length. Geochemical and isotopic studies indicated the Guojialing granodiorite was derived mainly from a crustal source, but with the involvement of mantle components (Yang et al., 2012). Mafic dikes intruded between 122 and 124 Ma (Yang et al., 2004). Most of the mafic dikes are fault controlled and share similar strikes with the gold orebodies or gold-bearing quartz veins. They are mainly composed of dolerite, hornblende dolerite and lamprophyre, and show ophitic and/or porphyritic-seriate textures, with phenocryst contents of 10–30%. The phenocrysts consist dominantly of clinopyroxene with subordinate plagioclase and phlogopite. The mineral assemblage of the matrix is similar to that of the phenocrysts but has a higher population of plagioclase. Previous studies suggested that the mafic dikes were derived from an enriched lithosphere mantle source (Yang et al., 2004).

The Sanshandao gold deposit is controlled by the Sanshandao–Cangshang fault zone, with the Linglong granite in the hanging wall and the Linglong granite/Guojialing granodiorite in the footwall (Fig. 2). This fault zone generally trends 35°, dips 35–40° southeast and extends to the northeast and southwest into the Bohai Sea. Structures along the fault zone are mainly characterized by brittle fracturing, throughout a zone of 50–200 m in width.

The alteration halos and orebodies generally trend northeast (20–40°), dip (35–70°) southeast, and extend offshore into the Bohai Sea (Fig. 2). Six orebodies, which are tabular or lenticular in shape and parallel to the main fault plane, have been identified. The No. 1 orebody accounts for 69% of the proven reserves, and lies within the middle to upper part of the pyrite–sericite–quartz alteration zone in the footwall of the main fault. This orebody is up to 1020 m in length, averages 6.4

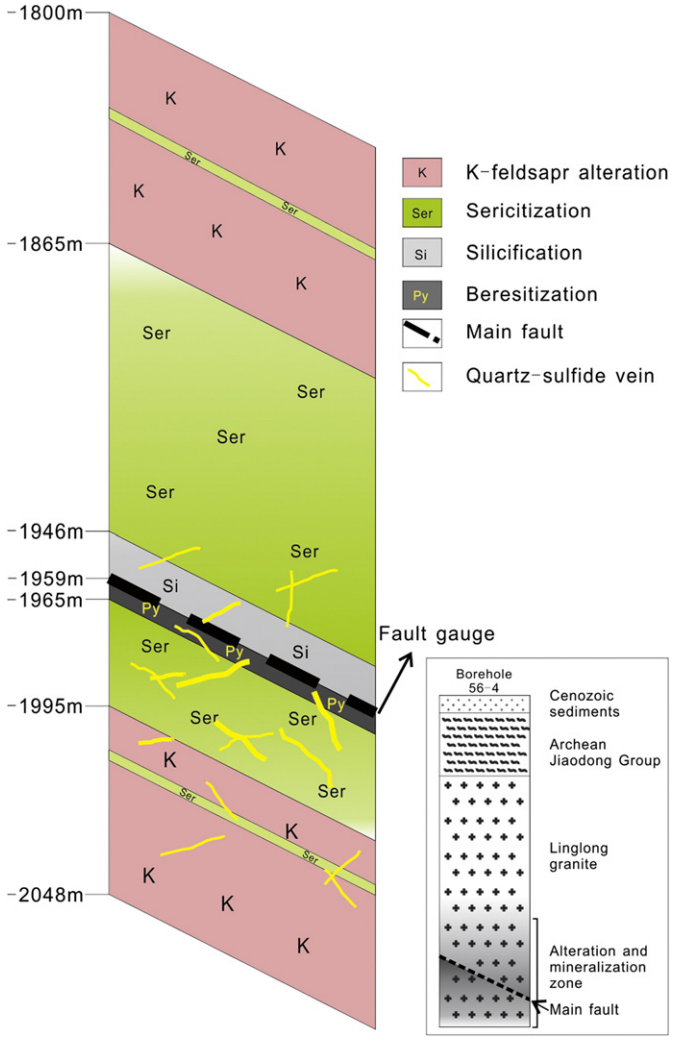

Fig. 3. Schematic sketch of the section showing the distribution of main alteration zones and veins near the regional fault. The insert is a schematic lithostratigraphic column revealed in the Borehole 56-4.

to 10.2 m in thickness, and continues to approximately 1450 m in depth, with mean grade of 2.92 g/t (maximum of 19.54 g/t). The No.2 orebody constitutes 30% of the proven reserves. It is located below the No. 1 orebody within the pyrite–sericite–quartz alteration zone, with a length of more than 560 m, and a thickness of 2.2–8.6 m. The grade of gold ores varies generally from 0.08 to 26.80 g/t, with an average at 2.84 g/t. Other orebodies comprise a little part of the proven reserves, so they are not described in detail in this paper. Two styles of gold mineralization are distinguished at the Sanshandao deposit: the most common style comprises disseminated gold within pyrite–sericite–quartz altered granitoids along the Sanshandao–Cangshang fault; small portion of gold bearing quartz vein/veinlet stockworks within the alteration halos comprises the other mineralization style.

So far, no direct age dating has been reported from the Sanshandao gold deposit. However, the nearby Cangshang deposit was dated at 121.3 ± 0.2 Ma (Zhang et al., 2003). The Xincheng, Jiaojia and Wangershan deposits, which are located in the same gold belt with the Sanshandao deposit (Fig. 1), were also dated as between 119.2 ± 0.2 and 121.0 ± 0.4 Ma (Li et al., 2004). Considering that the Sanshandao deposit shares very similar structural settings, ore mineralogy, alteration patterns and hydrothermal fluid compositions with these deposits, it is assumed that the Sanshaodao deposit also formed at about 120 Ma.

Samples for analysis in this study were collected mainly from Borehole 56-4, 96-2 and 96-3. These three boreholes are about 1500 m, 2100 m and 2200 m to the east of the Sanshandao gold deposit (Fig. 2), and have a drilling depth of 2050 m, 2030 m and 2025 m, respectively. Borehole 56-4 reveals that both hanging wall and footwall of the Sanshandao–Cangshang fault are occupied by the Linglong granite. The other two boreholes reveal that the hanging wall of the fault are the Linglong granite, whereas the footwall of the fault are the Guojialing granodiorite.

4. Methodology

Thin sections and polished blocks were prepared for petrographic study, and both optical and scanning electron microscopy observations were performed at the Institute of Geology and Geophysics, Chinese Academy of Sciences (IGGCAS).

The whole rock major and trace elements were determined for 20 samples from Borehole 56-4 at IGGCAS. For major element analyses, mixtures of whole-rock powder (0.5 g) and $Li_2B_4O_7 + LiBO_2$ (5 g) were heated and fused into glass disks and analyzed by X-ray fluorescence spectroscopy (XRF) with an AXIOS-Minerals spectrometer. The analytical uncertainties were generally within 0.1–1% (RSD). Loss on ignition (LOI) was obtained using 0.5 g powder heated up to 1100 °C for 1 h. For trace element analyses, whole-rock powders (40 mg) were dissolved in distilled HF + HNO_3 in Teflon screw-cap capsules at 200 °C for 5 days, dried, and then digested with HNO_3 at 150 °C for 1 day, and the final step was repeated. Dissolved samples were diluted to 49 ml with 1% HNO_3 and 1 ml 500 ppb indium was added to the solution as an internal standard. Trace element abundances were determined by inductively coupled plasma mass spectrometry (ICP-MS) using a Finnigan MAT ELEMENT spectrometer, which has analytical uncertainties within 5% for most elements.

Secondary K-feldspar, sericite and pyrite from the alteration and mineralization zones of Borehole 56-4 were selected for Sr–Nd isotopic analysis. The Rb–Sr and Sm–Nd isotopic analysis followed procedures similar to those described by Chu et al. (2009). Crushed samples were dissolved in a HF–$HClO_4$–HNO_3 mixture and spiked with appropriate amounts of mixed ^{87}Rb–^{84}Sr, ^{149}Sm–^{150}Nd tracer solution in Teflon bombs. Rb and Sr were separated using standard ion-exchange resins, and Sm and Nd were separated using Eichrom LN (LN-C-50B, 100–150 μm, 2 ml) chromatographic columns. They were analyzed on an IsoProbe-T thermal ionization mass spectrometer (GV Instruments, England), installed at the IGGCAS. The isotopic ratios were corrected for mass fractionation by normalizing to $^{86}Sr/^{88}Sr = 0.1194$ and $^{146}Nd/^{144}Nd = 0.7219$, respectively. The measured value for NBS987 Sr standard and JNdi-1 Nd standard were 0.710245 ± 10 (2σ, n = 12) and 0.512120 ± 11 (2σ, n = 12), respectively. Total procedural blanks are <40 pg for Rb, <300 pg for Sr, <25 pg for Sm, and <70 pg for Nd. USGS reference material BCR-2 was measured to monitor the accuracy of the analytical procedures, with the following results: $^{87}Sr/^{86}Sr = 0.704996 \pm 10$ (2σ, n = 12) and $^{143}Nd/^{144}Nd = 0.512636 \pm 11$ (2σ, n = 12).

The fault gouge from Borehole 56-4 was separated for XRD analysis at IGGCAS. XRD measurement was carried out on a D/MAX-2400 X-ray diffractometer, with CuKα radiation at 60 mA and 40 kV. The goniometer was equipped with a graphite monochromator in the diffracted beam. Data was collected in the angular range 3°–70° in 2θ, with 8°/min.

Phase-equilibrium calculation was carried out using the SUPCRT92 software package (Johnson et al., 1992), with an upgraded version of the database (slop98.dat). The thermodynamic properties for $Au(HS)_2^-$ are from Akinfiev and Zotov (2010). All other data are from the slop98.dat database. All the thermodynamic parameters for the thermal dynamic modeling were incorporated into SUPCRT92.

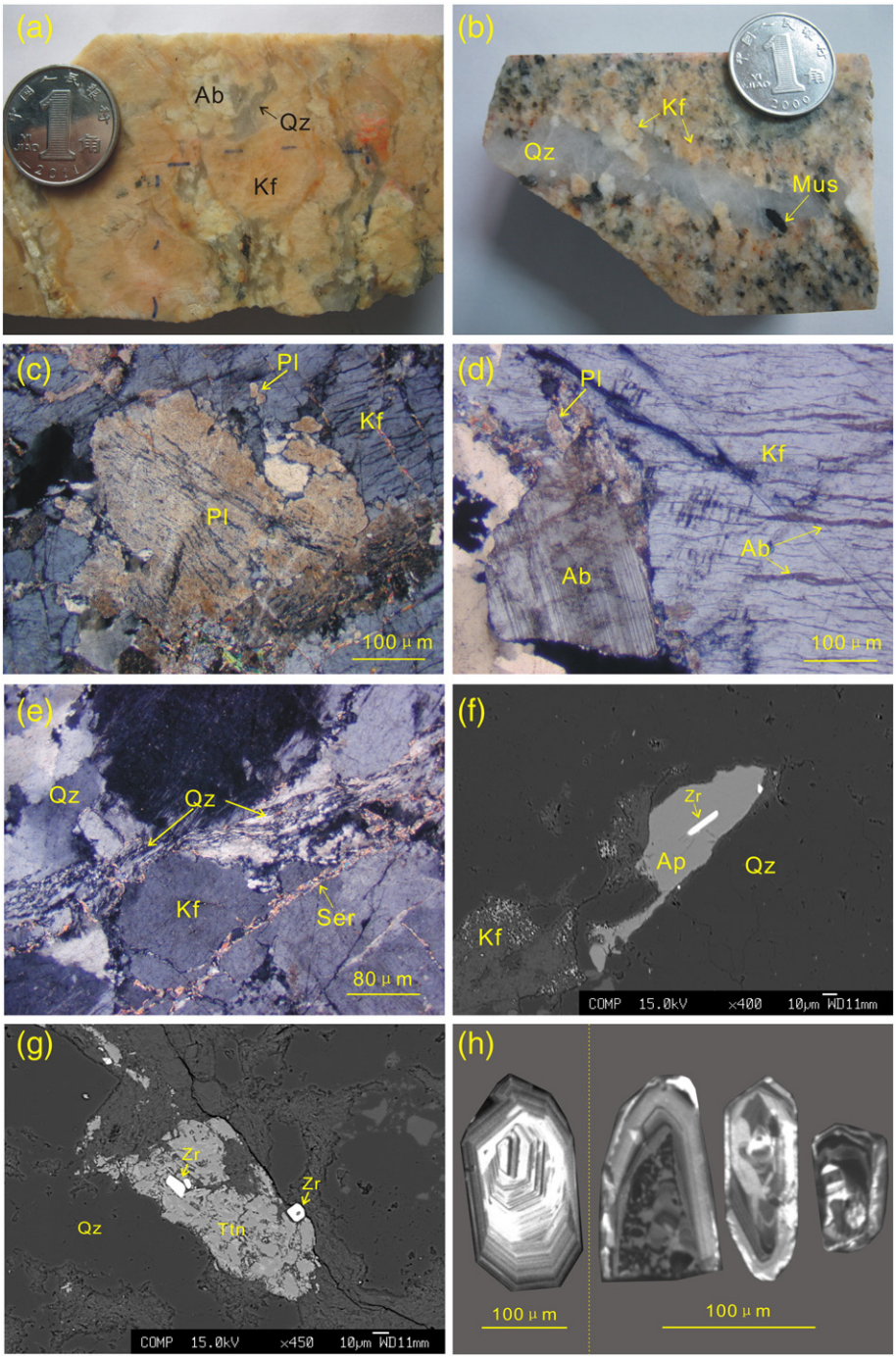

Fig. 4. Photographs (a and b), photomicrographs (c–e), backscattered electron images (f and g) and CL images of alteration assemblages associated with K-feldspar alteration. (a) K-feldspar alteration gives the rock a pinkish color. The main mineral assemblage is K-feldspar and quartz, with minor amounts of albite. (b) Quartz ± muscovite vein related K-feldspar alteration. Secondary K-feldspar crystals are mostly restricted to a narrow zone enveloping quartz ± muscovite vein. (c) Relict magmatic plagioclase is surrounded by secondary K-feldspar in weakly K-feldspar altered samples. (d) In heavily K-feldspar altered samples, magmatic plagioclase was almost totally replaced by K-feldspar; newly formed albite occurred among K-feldspar and quartz. Note that vermicular albite crystals are included in secondary K-feldspar. (e) Polycrystalline quartz ribbons surround the K-feldspar; K-feldspars show characteristics of slight brittle deformation, with sericite aggregates filling in the micro-fractures of K-feldspar. (f) Apatite grain replaced by quartz, and changing to anhedral. (g) Titanite grain and some zircon grains replaced by quartz and later sericite. (h) The zircon grain in left part is from the unaltered Linglong granite. It is euhedral and shows typical magmatic oscillatory zoning. Three zircon grains in the right part are from K-feldspar altered rocks. Note that they are subhedral and their inner textures were chaotic, maybe caused by hydrothermal alteration. Abbreviations: Kf—K-feldspar, Qz—quartz, Ab—albite, Pl—plagioclase, Mus—muscovite, Ser—sericite, Ap—apatite, Ttn—titanite, Zr—zircon.

5. Gold-related hydrothermal alteration, vein types and mineralization

Broad hydrothermal alteration halos of granitic wall rocks occur along the Sanshandao–Cangshang fault zone (Fig. 2), and regular spatial zonation of alteration and vein minerals can be observed (Fig. 3). Our petrographic studies reveal five major types of mineral assemblages. A fault gouge layer, which separates the hanging wall and footwall of the main fault, occurs in the innermost alteration zone. Below this layer, pyrite–sericite − quartz alteration occurs as the most intense alteration zone, and it is closely related to the gold mineralization. A relatively narrow silicification zone occurs above fault

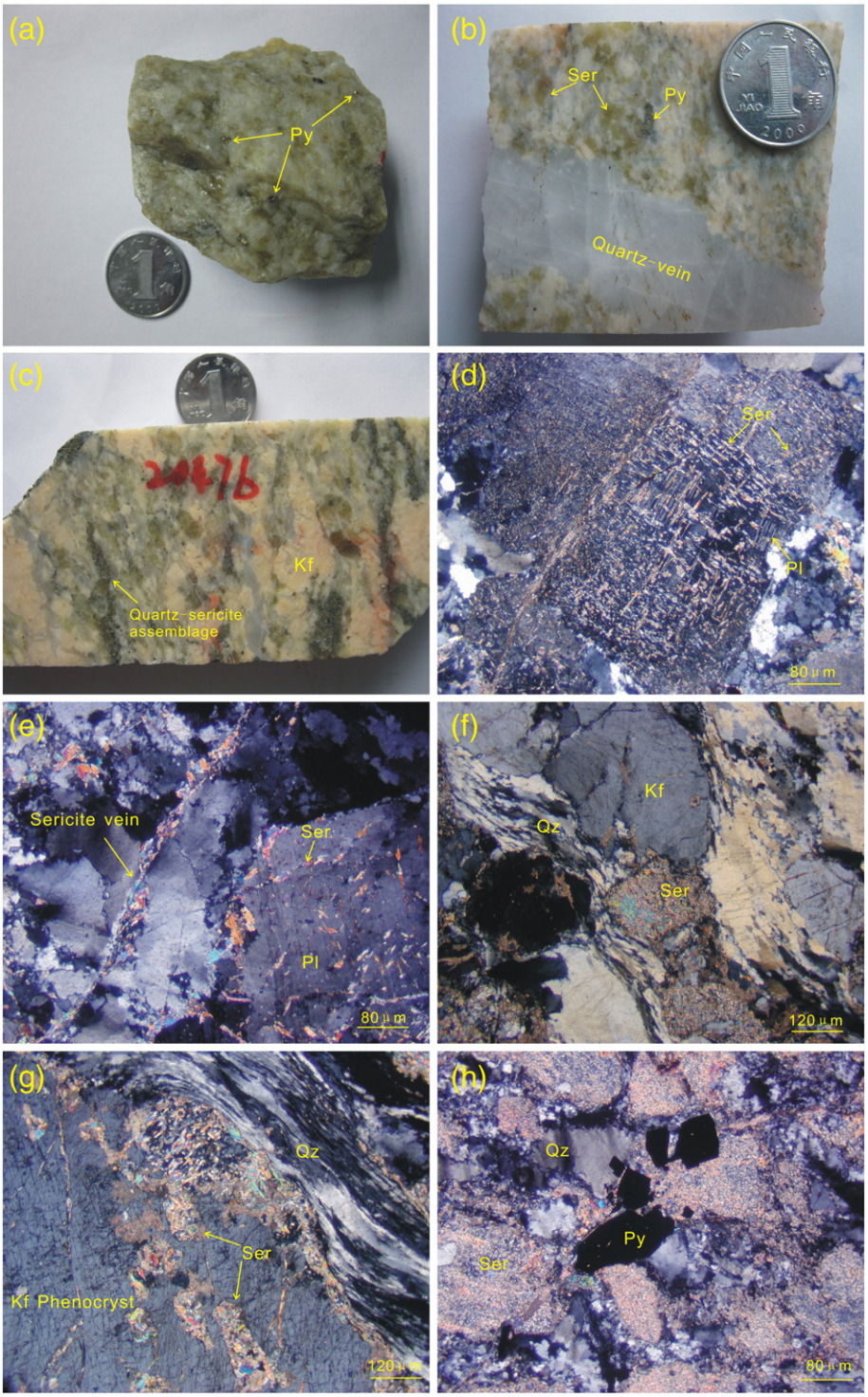

Fig. 5. Photographs (a–c) and photomicrographs (d–h) of alteration assemblages associated with sericitization. (a) Heavy sericitization gives the rock a green color. The main mineral assemblage is sericite, quartz and K-feldspar, with trace disseminated pyrite. (b) Quartz-vein related sericitization. Plagioclase grains were locally replaced by sericite and quartz. Pyrite also occurred as disseminated aggregates. (c) K-feldspar alteration was overprinted by sericitization. (d) Plagioclase crystals were replaced by sericite along polysynthetic twinning. (e) Sericite did not only locally replace plagioclase, but also formed thin veinlets filling in fractures. (f) Plagioclase crystals were totally replaced by sericite, whereas K-feldspar crystals were retained. Polycrystalline quartz ribbons occurred among other secondary minerals. (g) Plagioclase crystals included in magmatic K-feldspar phenocryst from the Guojialing granodiorite were totally transformed into sericite, but K-feldspar underwent little alteration. Polycrystalline quartz ribbons surround the K-feldspar phenocryst. (h) Sericite aggregates retain pseudomorphs of plagioclase. Pyrite occurs as disseminated grains. Abbreviations: Py—pyrite, other abbreviations are as in Fig. 4.

gouge in the hanging wall. Both pyrite — sericite — quartz alteration in the footwall and silicification in the hanging wall are enveloped by variable intensities of diffusive sericitization. K-feldspar alteration typically occupies the outermost part of alteration halos, but a few relatively narrow discrete sericitization zones develop along fractures in K-feldspar alteration zone. Minor amounts of sodic (albite) alteration, carbonation and argillic alteration are also observed. Because of the scarcity of their distribution, they are not described in detail

in this paper. Similar to the other typical Jiaojia-type gold deposits, quartz-sulfide veins/veinlets are less developed in the Sanshandao deposit, and occur mainly in alteration halos in the footwall.

5.1. K-feldspar alteration

K-feldspar alteration occurs in the outermost part of the alteration zone, and generally developed along brittle fractures in the granitic wall rocks. The alteration is well developed (50–60 m in thickness) in Borehole 56-4, whereas it is only locally noticed in the other two boreholes and the Sanshandao deposit itself. K-feldspar alteration usually gives the rocks a pinkish appearance (Fig. 4a), which is commonly believed to be due to hematitic dusting (Plümper and Putnis, 2009; Putnis et al., 2007).

K-feldspar alteration is irregular in intensity and generally diffuse. Weakly altered rocks are characterized by relict plagioclase within secondary K-feldspar (Fig. 4c), partial or total transformation of biotite to muscovite and magnetite. With strong K-feldspar alteration, the original igneous texture was largely obliterated, with secondary K-feldspars totally replacing plagioclase (Fig. 4d), biotite disappeared, and minor secondary albite and muscovite occurred together with the secondary K-feldspar crystals (Fig. 4d). The secondary K-feldspar crystals are anhedral and large (1–4 cm in size) (Fig. 4a). Patch or vermicular albite crystals are included in the K-feldspar (Fig. 4d). Secondary quartz, replacing plagioclase, is also a very common part of both weak and strong K-feldspar alteration assemblage. Quartz grains mainly occur as polycrystalline quartz ribbons surrounding the K-feldspar crystals, indicating that they have experienced ductile deformation (Fig. 4e). Only limited sulfide minerals are associated with K-feldspar alteration. With increasing alteration intensity, the accessory minerals, such as apatite and titanite, are also gradually replaced by quartz (Fig. 4f and g). Most of these minerals show a decrease in grain size and become increasingly anhedral. Zircons, which are traditionally assumed to be resilient to hydrothermal alteration, also become smaller and anhedral. As seen from CL images, the inner textures of zircons were largely altered by hydrothermal fluids (Fig. 4h).

A very small portion of the K-feldspar alteration is related to quartz ± muscovite veins (Fig. 4b). These veins have halos of K-feldspar crystals, which are anhedral, relatively large (0.5–2 cm in size) and contain some vermicular albite. Quartz crystals in the vein occur as recrystallized sub-grains. Very minor amounts of muscovite aggregates also occur in the vein. No clear timing relationships have been observed between vein related and diffusive K-feldspar alteration, but similar mineral assemblages and petrographic characteristics of K-feldspar suggest that they were probably contemporaneous.

5.2. Sericitization

Large scale (about 100 m in thickness) diffusive sericitization symmetrically developed across the fault zone, and is marked by green to white colors (Fig. 5a). The intensity of the diffusive sericitization generally decreases from inner to outer parts of the alteration zone. Towards the outer part, the sericitization generally took place along brittle fractures. Borehole 56-4, 96-2 and the Sanshandao deposit itself reveal that rocks in the footwall experienced stronger sericitization than those in the hanging wall. However, the samples from Borehole 96-3 show that wall rocks in the hanging wall also underwent strong diffusive sericitization.

With weak diffusive alteration, biotite was partly or totally replaced by sericite, and plagioclase crystals were converted to sericite along

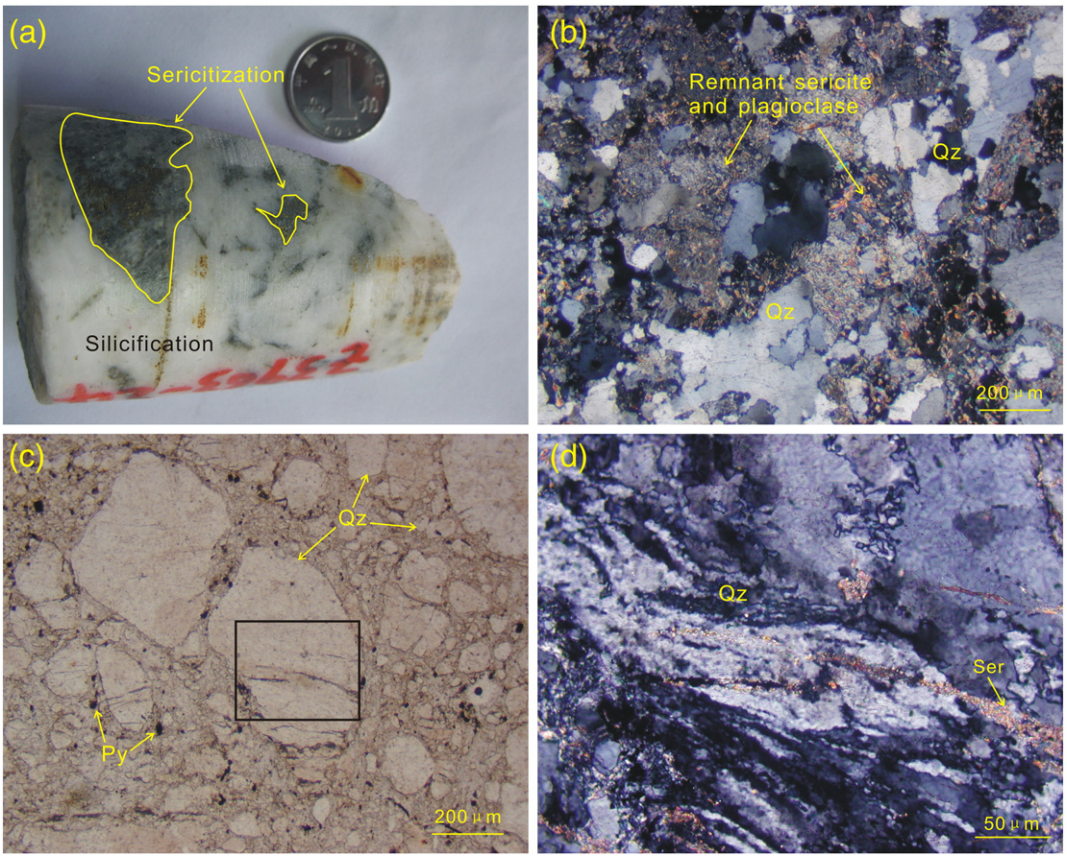

Fig. 6. Photographs (a) and photomicrographs (b, c and d) of alteration assemblages associated with silicification. (a) Sericitization was severely overprinted by white quartz aggregates. (b) Sericite and plagioclase in the earlier stage were replaced by quartz. (c) Angular quartz ± feldspar fragments of variable sizes are present in deformed silicified rock. (d) Magnification of box area in Fig. 6c, showing a single quartz porphyroclast consisting of elongated sub-grains. Abbreviations are as in Figs. 4 and 5.

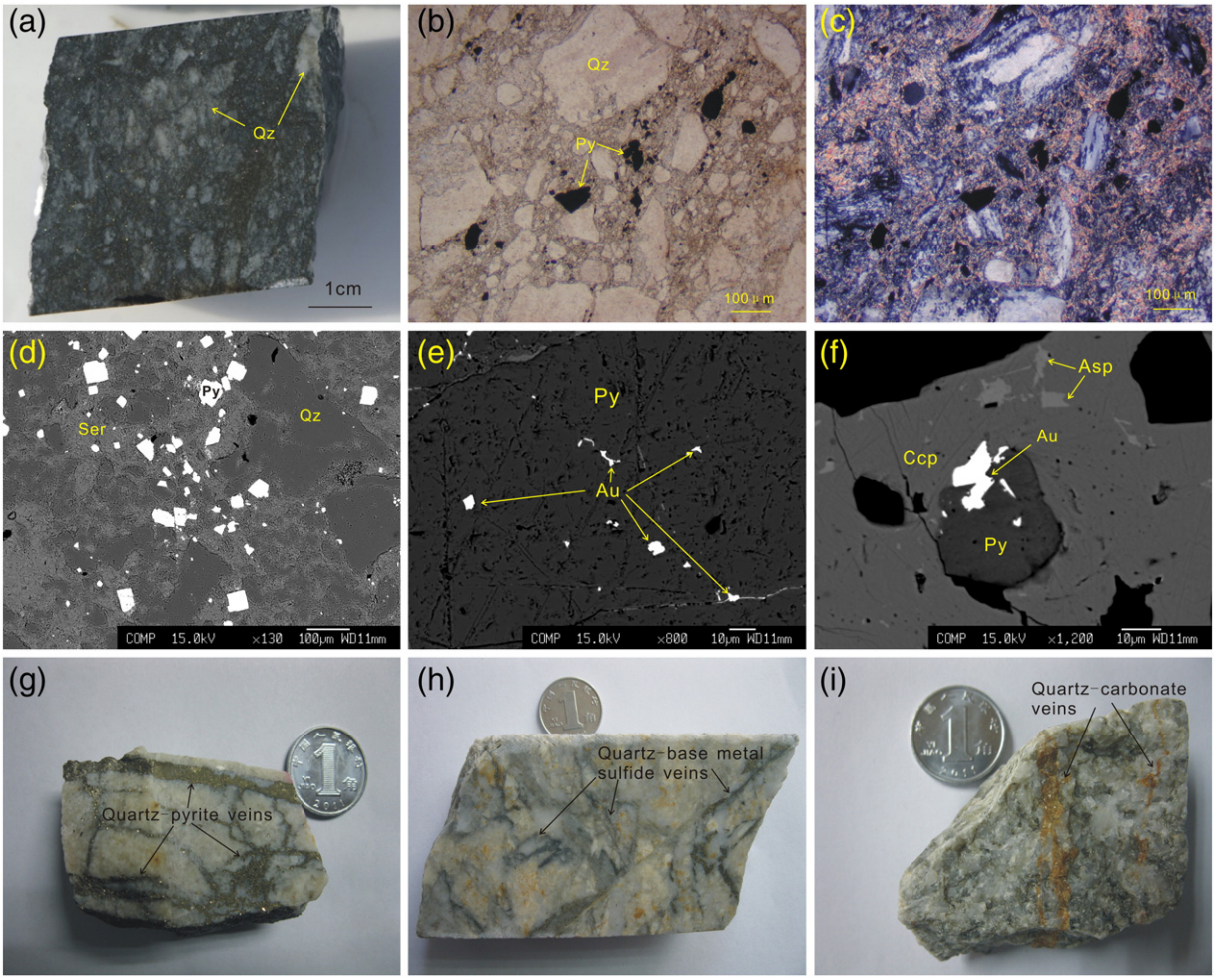

Fig. 7. Photographs (a and g–i), photomicrographs (b and c) and backscattered electron images (d–f) showing mineral assemblages and veins associated with pyrite–sericite–quartz alteration and occurrence of gold. (a) Pyrite–sericite–quartz altered samples are black. White quartz fragments are visible. Pyrite–sericite–quartz alteration took place along open spaces of breccia. (b) and (c) The same area under plane polarized light and perpendicular polarized light, respectively. Quartz fragments exhibit irregular shapes and various sizes. Most single quartz porphyroclasts consist of elongated sub-grains. Sericite generally appears as veinlets filling fissures. Pyrite grains are disseminated in rocks. (d) Disseminated pyrite grains are euhedral to subhedral, and show various sizes. Sericite appears as disseminated grains intergrown with fine grained quartz. (e) Irregular gold grains occur as inclusions or infillings in pyrite. (f) Anhedral gold grain is included in pyrite and chalcopyrite. Arsenopyrite grains are also included in chalcopyrite. (g) Quartz–pyrite veins cut silicified sample. (h) Quartz–base metal sulfide veins, which are gray in color, overprint former K-feldspar alteration. (i) Quartz-carbonate veins overprint former sericitization. Abbreviations: Au—gold, Ccp—chalcopyrite, Asp—arsenopyrite, other abbreviations are as in Figs. 4 and 5.

hairline cracks or polysynthetic twinning, although the twinning and zoning are still visible (Fig. 5d and e). K-feldspar crystals underwent little alteration. With strong diffusive sericitization, sericite replaced all the plagioclase and biotite, retaining pseudomorphs of plagioclase (Fig. 5f, g and h). Minor portion of the K-feldspar crystals were converted into sericite (Fig. 5f and g). In both weakly and strongly altered rocks, sericite

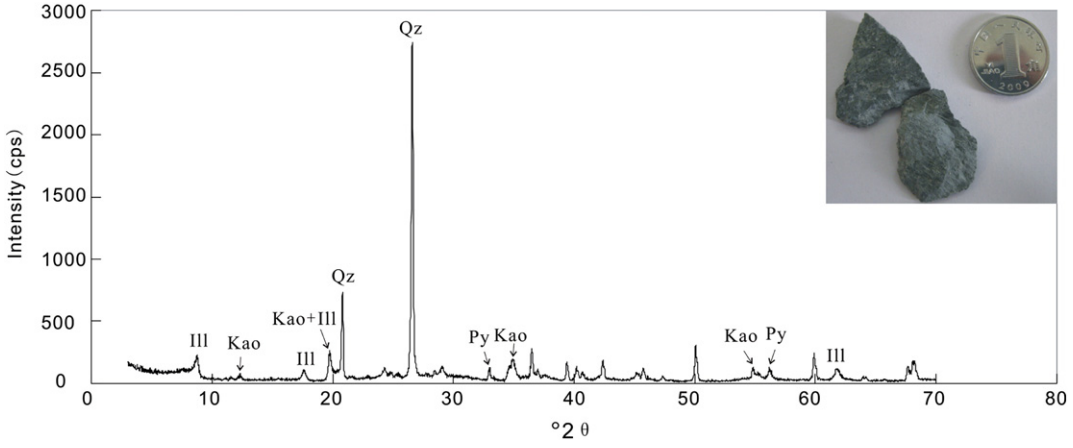

Fig. 8. X-ray diffraction patterns of fault gouge. The inset shows image of fault gouge. Abbreviations: Qz—quartz, Kao—kaolinite, Ill—illite, Py—pyrite.

not only replaced feldspars locally, but also formed as thin veinlets filling in micro-fractures (Figs. 4e and 5e). A small amount of sulfide minerals, mainly pyrite, as disseminated grains are also a ubiquitous part of the diffusive sericitization assemblages (Fig. 5h). Quartz crystals in this alteration zone also display features of ductile deformation (Fig. 5f and g).

A minor portion of sericitization was quartz-vein related, and is mainly composed of sericite, with subordinate pyrite. Adjacent to the quartz-vein, sericite locally replaced plagioclase, or appeared as thin veinlets among other crystals, and pyrite occur as euhedral cubes or subhedral aggregates (Fig. 5b). Quartz in the vein appears as elongated sub-grains. Vein-related sericitization shares similar alteration mineral assemblage with diffusive sericitization, indicating that they were broadly contemporaneous.

In macro-scale, it is clear that sericitization overprints K-feldspar alteration (Fig. 5c), especially along fractures in the K-feldspar alteration zone. In micro-scale, sericite appears as thin veinlets filling micro-fractures in secondary K-feldspar crystals (Fig. 4e). Therefore, sericitization is inferred to be later than K-feldspar alteration.

5.3. Silicification

The three boreholes (56-4, 96-2 and 96-3) reveal that a relatively narrow silicification zone (5–20 m in thickness) occurs above the fault gouge layer in the hanging wall, and varies from white to green in color (Fig. 6a). As with sericitization, the intensity of silicification generally decreases away from the center of the main fault. With weak silicification, parts of former altered rocks were replaced by quartz, with remnant K-feldspar, sericite, plagioclase and sulfide surrounded by newly formed quartz (Fig. 6b). Strong silicification replaced most former minerals by quartz. Small amounts of sericite and sulfide precipitated together with secondary quartz. Most silicified rocks, especially those near the main fault, sustained strong brittle deformation. Angular quartz ± feldspar fragments of variable size are present (Fig. 6c). It is noted that most single quartz porphyroclast consist of elongated quartz sub-grains (Fig. 6d), indicating that ductile deformation of quartz had occurred before strong brittle deformation.

The contact between the silicification and sericitization zones is gradational, but in both macro- and micro-scale it is clear that silicification overprinted sericitization (Fig. 6a and b). Therefore, the timing of silicification may have overlapped with, or more probably largely postdated, that of sericitization.

5.4. Pyrite–sericite–quartz alteration, veins and gold mineralization

Boreholes expose that a ca. 5–15 m thick pyrite–sericite–quartz alteration zone occurs nearest to the fault gouge in the footwall of the main fault, and is characterized by black to dark green in color (Fig. 7a). As with silicified rocks mentioned above, rocks in this zone are also cataclastic breccias formed during brittle deformation. Strong pyrite alteration, sericitization and silicification, which heavily overprinted former sericitization and silicification, developed along cracks or other open spaces of breccias (Fig. 7a, b and c). This zone mainly comprises quartz, sericite and pyrite. Most quartz grains are porphyroclasts, exhibiting irregular shapes and various sizes (Fig. 7a, b and d). Most single quartz porphyroclasts are aggregates of former dynamically recrystallized sub-grains (Fig. 7c). A small portion of quartz, especially those fine grained crystals, may have been derived from hydrothermal alteration. Sericite generally appears as veinlets filling

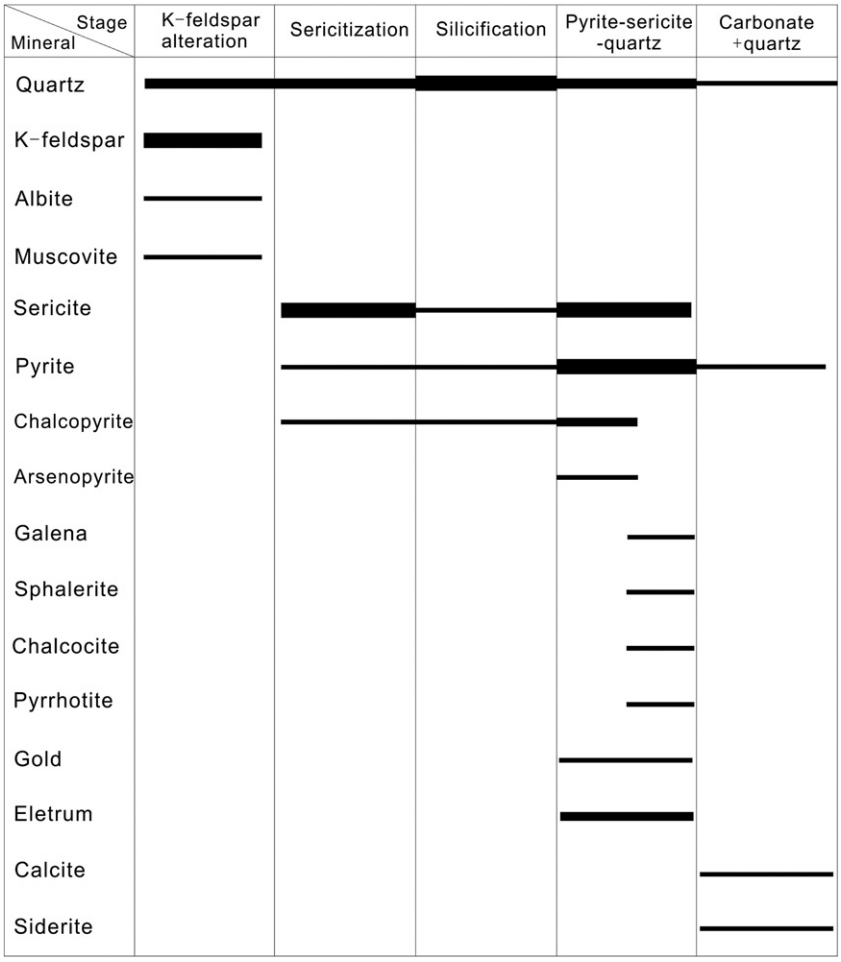

Fig. 9. Paragenetic sequence for the hydrothermal minerals of the Sanshandao gold deposit. The widths of the solid lines denote relative abundance of minerals.

Table 1
Major oxides (wt.%) and trace elements (ppm) for the Linglong granite and altered samples.

Rock-type	Linglong granite		K-feldspar alteration					
Sample	L-1545 m	L-1899 m	K-1805 m	K-1839 m	K-1862 m	K-1995 m	K-2047 m	K-2048 m
SiO_2	72.24	70.72	70.73	70.63	73.67	70.71	72.79	70.52
TiO_2	0.13	0.18	0.03	0.01	0.03	0.02	0.12	0.04
Al_2O_3	14.98	15.90	15.13	15.54	14.36	15.77	13.74	16.00
FeO	1.31	1.36	0.55	0.24	0.51	0.39	1.22	0.50
MgO	0.14	0.22	0.08	0.04	0.05	0.06	0.09	0.05
CaO	1.46	1.57	1.36	0.26	0.73	0.87	0.98	1.44
Na_2O	4.76	5.03	3.35	1.60	3.84	3.32	2.62	4.78
K_2O	3.83	3.93	7.39	11.35	6.16	8.03	6.97	5.13
P_2O_5	0.03	0.04	0.01	0.01	0.01	0.01	0.01	0.01
LOI	0.56	0.66	1.36	0.34	0.52	0.88	1.00	0.98
Total	99.44	99.61	99.99	100.02	99.88	100.06	99.54	99.45
Sc	1.61	1.29	1.25	0.36	2.16	0.57	0.69	0.86
V	7.8	6.6	5.2	5.2	2.2	1.5	8.3	1.9
Cr	172	265	160	117	224	150	160	113
Co	2.2	1.8	1.4	1.5	1.6	1.0	1.8	0.9
Ni	4.8	4.5	4.8	0.1	6.2	2.1	1.7	2.9
Cu	1.9	2.1	3.0	0.4	2.0	1.6	9.7	1.8
Zn	33	12	4	2	5	2	7	2
Ga	22	24	26	23	31	24	15	28
Rb	115	90	247	349	216	192	121	117
Sr	599	456	233	67	103	243	518	262
Y	7.7	4.6	8.7	1.4	5.8	0.4	0.4	0.9
Zr	83	127	15	4	49	4	11	30
Nb	6.4	11.6	3.0	1.1	10.5	0.7	2.6	2.6
Cs	1.7	1.5	0.7	3.3	2.2	1.7	0.6	1.0
Ba	1371	1765	602	300	217	586	2491	577
La	18.3	14.7	7.0	2.6	6.5	0.3	0.7	0.5
Ce	30.0	24.3	12.3	4.1	13.0	0.3	0.7	0.6
Pr	3.62	3.12	1.54	0.67	2.04	0.03	0.08	0.06
Nd	13.2	11.3	6.7	2.9	9.4	0.1	0.3	0.3
Sm	2.4	2.3	2.0	0.7	2.8	0.0	0.1	0.1
Eu	0.46	0.35	0.31	0.24	0.27	0.15	0.46	0.25
Gd	1.88	1.71	1.88	0.55	2.40	0.05	0.10	0.10
Tb	0.28	0.22	0.31	0.07	0.29	0.01	0.01	0.02
Dy	1.37	0.92	1.75	0.35	1.32	0.05	0.09	0.14
Ho	0.26	0.14	0.31	0.05	0.23	0.01	0.02	0.03
Er	0.64	0.37	0.79	0.13	0.52	0.03	0.06	0.10
Tm	0.10	0.06	0.11	0.02	0.07	0.01	0.01	0.02
Yb	0.61	0.37	0.65	0.09	0.43	0.05	0.08	0.14
Lu	0.10	0.06	0.09	0.01	0.07	0.01	0.01	0.03
Hf	2.7	4.2	1.1	0.3	3.9	0.2	0.4	2.2
Ta	0.41	0.70	0.20	0.05	0.98	0.19	0.12	0.19
Pb	31	24	30	69	50	48	26	29
Bi	0.01	0.01	0.00	0.02	0.04	0.01	0.01	0.00
Th	5.8	3.6	6.5	10.3	10.8	0.6	0.2	3.0
U	1.93	1.10	2.85	1.02	8.15	2.24	0.27	12.37
Zr/Hf	30.77	30.14	14.00	14.44	12.41	18.41	26.72	14.11
Y/Ho	29.56	32.77	28.11	26.67	25.70	34.64	17.48	28.91
Nb/Ta	15.38	16.58	15.08	21.45	10.71	3.74	21.50	13.93
δEu	0.64	0.53	0.48	1.15	0.30	10.93	14.67	8.46
∑Ree	73.17	59.80	35.78	12.58	39.37	1.19	2.68	2.36

fissures (Fig. 7c), or as disseminated grains coexisted with fine grained quartz (Fig. 7d). Pyrite is the most common sulfide mineral in this zone, and occurs as euhedral to subhedral grain ranging from 10 to 500 μm in size (Fig. 7d). They are disseminated within the rocks, or occur as pyrite ± sericite ± quartz stockworks. In addition to pyrite, minor amounts of chalcopyrite (Fig. 7f) and little galena, sphalerite, arsenopyrite, chalcocite and pyrrhotite can also be found, typically as micro-crack fillings or inclusions in pyrite. They probably precipitated contemporaneously with disseminated pyrite and pyrite stockworks.

The gold mineralization is closely associated with pyrite–sericite–quartz alteration. Gold occurs mostly as electrum, with minor amounts of native gold. Gold grains are anhedral and range from 10 to 100 μm in size. Most of the electrum and native gold grains are spatially associated with pyrite, occurring as inclusions or infillings in pyrite (Fig. 7e and f). Less commonly, gold also occurs as small inclusions in quartz or as individual grains along cleavage planes in sericite.

Quartz-sulfide veins/veinlets, which were largely contemporaneous with pyrite–sericite–quartz alteration, can be observed in alteration halos, especially in the footwall. It is noted that the Sanshandao deposit itself contains more veins/veinlets than the three other observed boreholes (56-4, 96-2 and 96-3). Based on mineral assemblages, two types of veins can be distinguished: quartz–pyrite veins and quartz–base metal sulfide veins. The quartz–pyrite veins consist of quartz and pyrite, with minor chalcopyrite and arsenopyrite (Fig. 7g). Quartz occurs as white–gray aggregates, and pyrite occurs as coarse euhedral cubes and subhedral aggregates. The quartz–base metal sulfide veins are characterized by precipitation of gray quartz and different types of fine-grained anhedral sulfide minerals (e.g. pyrite, chalcopyrite, arsenopyrite, galena, sphalerite and so on) (Fig. 7h). Gold occurs as inclusions or crack fillings within sulfide minerals.

Late stage quartz-carbonate veins cut all other stages. They are composed mainly of quartz, calcite and siderite, with subordinate pyrite

Sericitization						Silicification		Pyrite–sericite–quartz alteration			
S-1968 m	S-1973 m	S-1975 m	S-2000 m	S-2003 m	S-2020 m	Si-1948 m	Si-1957 m	psq-1959 m	psq-1961 m	psq-1962 m	psq-1962 m-b
71.48	70.09	73.45	73.15	76.16	71.06	76.99	84.21	74.86	68.37	65.57	73.77
0.15	0.13	0.20	0.16	0.12	0.21	0.03	0.06	0.09	0.14	0.16	0.08
13.58	15.70	14.58	16.17	14.63	15.31	12.43	8.70	9.20	12.08	12.49	10.64
0.81	0.95	1.14	0.65	0.72	0.89	0.76	1.92	6.46	8.49	9.39	6.31
0.24	0.15	0.24	0.19	0.17	0.24	0.06	0.51	0.57	0.39	0.50	0.34
3.91	2.96	1.85	1.15	1.20	2.42	1.17	0.21	1.58	0.09	0.39	0.10
0.11	0.13	0.15	0.18	0.12	0.21	4.70	0.12	0.07	0.05	0.06	0.05
4.05	4.61	5.09	5.81	4.34	5.66	2.63	2.99	2.88	3.98	4.53	3.41
0.03	0.02	0.04	0.03	0.03	0.04	0.01	0.01	0.03	0.03	0.05	0.02
4.96	4.32	3.08	2.70	2.78	3.60	0.98	1.84	4.75	5.73	6.23	4.67
99.32	99.06	99.82	100.19	100.27	99.64	99.76	100.57	100.50	99.35	99.36	99.40
0.69	1.06	2.03	1.29	1.38	1.68	0.54	3.81	1.57	1.19	1.29	1.10
11.5	6.2	3.7	3.5	5.9	4.0	4.1	34.6	21.3	19.8	12.0	5.0
92	176	177	196	140	221	289	228	191	243	195	200
1.5	1.8	1.5	1.5	1.8	1.8	1.6	2.2	2.8	3.0	7.9	1.8
2.0	1.7	4.1	4.3	3.4	8.3	7.2	6.0	8.9	5.8	5.8	4.5
16.0	4.6	3.8	2.7	22.7	28.4	10.6	190.7	16.4	47.0	87.5	109.0
140	10	55	62	205	54	3	11	25	10	8	15
16	21	20	17	15	19	21	39	12	14	18	12
97	114	122	128	103	117	58	127	103	133	148	114
514	316	259	226	118	420	102	42	226	11	64	14
4.2	4.0	4.2	2.0	3.2	4.1	1.8	1.4	3.6	2.9	3.2	2.4
97	104	118	127	117	129	30	33	37	59	56	43
3.8	5.1	4.9	3.0	5.3	4.4	1.8	4.4	6.0	3.3	2.7	3.7
1.1	1.2	0.6	1.0	0.8	1.5	0.3	1.2	1.5	0.8	0.8	0.7
1489	1097	1268	1780	831	2456	235	200	477	211	591	211
13.6	12.7	18.9	32.2	11.4	33.6	2.5	1.7	18.2	22.6	30.7	19.4
22.6	20.1	28.5	51.1	18.0	51.1	3.3	2.9	29.7	36.9	51.3	32.3
2.41	2.28	3.57	6.18	2.09	6.13	0.53	0.34	3.29	4.05	5.64	3.41
8.4	8.1	11.5	21.6	7.3	20.5	2.0	1.3	12.2	13.9	20.9	12.5
1.4	1.4	2.0	2.9	1.2	3.2	0.4	0.3	2.2	2.1	2.7	2.0
0.91	0.80	0.51	0.42	0.42	0.55	0.19	0.15	0.79	0.48	1.03	0.45
1.04	1.14	1.33	1.66	0.86	2.00	0.30	0.33	1.62	1.44	1.99	1.39
0.16	0.15	0.18	0.17	0.13	0.24	0.06	0.05	0.22	0.17	0.22	0.17
0.87	0.86	0.93	0.72	0.73	1.10	0.38	0.31	0.96	0.69	0.86	0.64
0.17	0.17	0.18	0.12	0.15	0.19	0.09	0.06	0.12	0.09	0.10	0.10
0.47	0.45	0.50	0.29	0.41	0.47	0.25	0.15	0.31	0.28	0.24	0.35
0.08	0.07	0.07	0.04	0.06	0.07	0.03	0.02	0.05	0.03	0.04	0.04
0.52	0.50	0.48	0.25	0.43	0.44	0.20	0.15	0.31	0.20	0.27	0.28
0.09	0.09	0.08	0.04	0.08	0.08	0.03	0.02	0.06	0.03	0.03	0.04
3.4	4.1	3.4	3.6	4.0	3.7	1.2	1.2	1.3	1.6	1.4	1.5
0.17	0.34	0.21	0.13	0.20	0.21	0.17	0.19	1.13	0.69	0.45	0.36
17	24	42	134	67	31	14	126	54	143	13	439
0.01	0.03	0.03	0.02	0.01	0.01	0.01	0.73	6.78	11.80	21.50	23.00
3.5	3.0	4.4	6.1	2.5	7.8	2.8	1.9	4.6	4.3	4.8	3.5
1.05	1.22	0.85	0.32	0.42	0.59	1.88	1.02	4.11	1.13	1.03	1.13
28.45	25.39	35.14	35.02	29.40	34.67	24.94	28.33	27.82	36.88	39.16	28.48
24.70	23.97	23.10	17.02	21.55	21.84	20.79	25.25	30.08	31.89	33.44	25.15
22.66	15.09	23.68	23.80	26.84	21.23	10.56	22.67	5.34	4.76	5.94	10.25
2.22	1.85	0.91	0.54	1.22	0.62	1.69	1.42	1.22	0.79	1.30	0.79
52.66	48.84	68.77	117.67	43.20	119.69	10.18	7.80	70.04	82.98	116.02	73.00

(Fig. 7i). In some cases, veins/veinlets of only calcite or siderite are displayed.

5.5. Fault gouge

The black-colored fault gouge with a thickness of 10–30 cm mainly consists of very fine grained quartz, illite, kaolinite, with minor pyrite (Fig. 8). Besides, amorphous phases are also detected by XRD analysis. The fault gouge may largely form in response to the movements along the Sanshandao–Cangshang fault, which also led to strong brittle deformation near the main fault as mentioned above.

It is noted that in almost all Jiaojia-type gold deposit, the gold orebodies occur in main fault footwalls parallel to the fault planes (Fan et al., 2005; Li and Yang, 1993; Qiu et al., 2002). Therefore, it is assumed that the fault gouge mainly formed before the major gold mineralization event, acting as a “barrier layer” that is impermeable for fertile ore-forming fluid to move upward, so that the gold was only precipitated in the footwall (Qiu et al., 2002).

5.6. Summary on paragenetic sequence of alteration, veins and mineralization

Based on field and microscopic investigations, five stages of alteration assemblages have been identified (Fig. 9). Activities of the Sanshandao–Cangshang fault created permeability which allows hydrothermal fluids to infiltrate wall rocks, leading to diffusive K-feldspar alteration on two fault planes. Pervasive sericitization followed and overprinted K-feldspar alteration. Subsequently, small scale silicification occurred, mainly overprinting sericitization. Later, reactivation of the main fault led to strong brittle deformation and the formation of fault gouges, which prevented later fluids from moving upward. After the formation of fault gouges, pyrite–sericite–quartz alteration occurred during the most intense phase of hydrothermal alteration, strongly overprinting

former sericitization and silicification in the footwall of the main fault. Gold mineralization was closely related to pyrite–sericite–quartz alteration. Quartz–pyrite and quartz–base metal sulfide veins/veinlets also developed during pyrite–sericite–quartz alteration stage. The latest stage quartz-carbonate/carbonate veins mark the waning of gold-related hydrothermal activity.

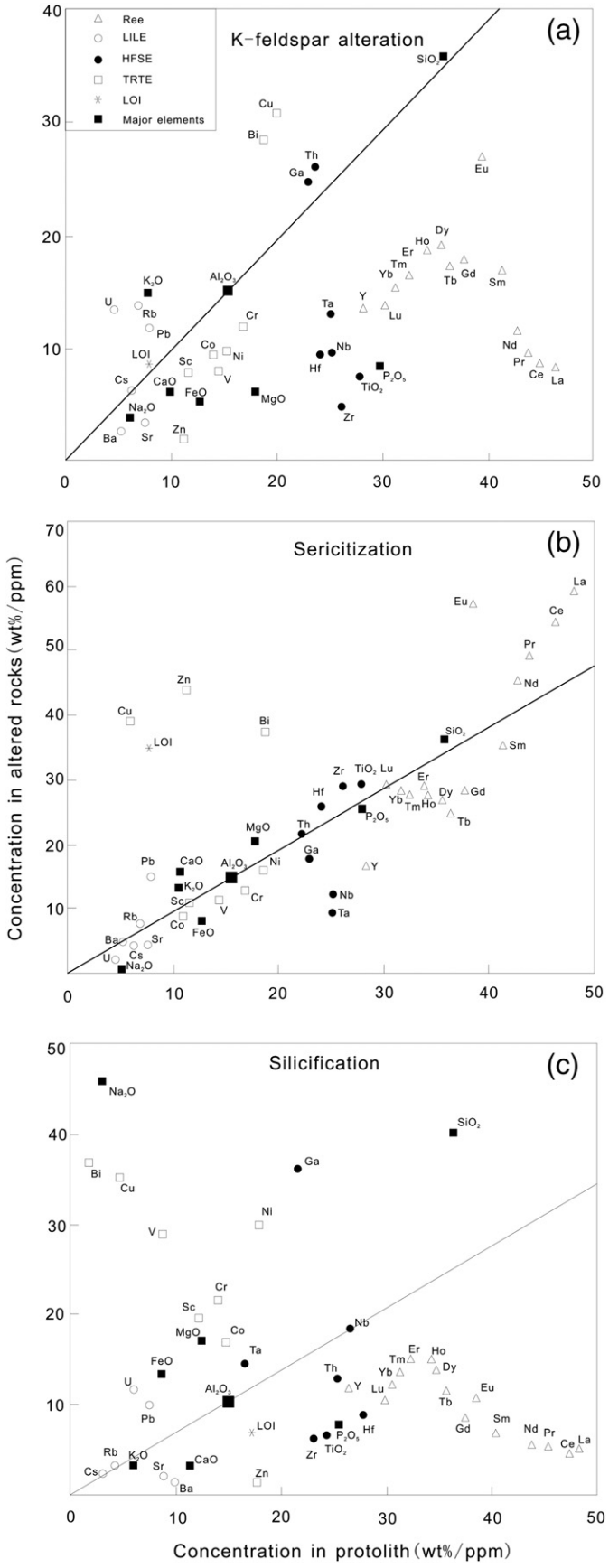

Fig. 10. Isocon diagrams in which the "protolith" (the Linglong granite and, in the case of silicification, samples undergone sericitization) versus the altered samples are plotted. Various elements are multiplied or divided by a constant to improve the graphical effects; this process would not affect the validity in illustrating the mass transfer characters (Grant, 1986). Black lines (isocons) are defined by the constant ratios of immobile elements (Al_2O_3), which were used for the calculation of the gains and losses. Elements above these lines are enriched in the altered rock, whereas elements below the lines are depleted during alteration.

6. Bulk-rock geochemistry and mobilization of elements

To estimate the chemical changes associated with the main alteration assemblages, the major elements (Si, Al, Fe, Mg, Ca, Na, K and P), rare-earth elements (REEs), light-lithophile elements (LILEs; e.g., Cs, Rb, Sr, Ba, Pb and U; Schilling, 1973), high-field strength elements (HFSEs; e.g., Nb, Ta, Ti, Zr, Hf, Th and Ga; Panahi et al., 2000) and trans-transition elements (TRTEs; e.g., Sc, V, Cr, Co, Ni, Cu, Zn and Bi; Jenner, 1996) were analyzed in representative samples of altered rocks and their equivalent, least altered "protoliths" (Table 1). Our sample selection for geochemical analysis ensured representation of a specific alteration assemblage and without any obvious open-space filling veins to overcome the problem of alteration overprinting.

The isocon method of Grant (1986) was used to demonstrate potential chemical changes between altered wall rocks and their corresponding "protoliths" (Fig. 10a, b and c). In this paper, we choose Al_2O_3 as the most immobile reference element during construction of isocons. Element gains and losses on a weight basis have been calculated following Grant's approach (Grant, 1986) and using Al_2O_3 as the immobile element:

$$\Delta C = \left(C^{F}{}_{immobile}/C^{A}{}_{immobile}\right) \cdot C^{A} - C^{F}$$

where C^F and C^A are the concentrations in the fresh (F) and altered (A) sample, respectively, and ΔC denotes the gain or loss in grams per 100 g of rock for major elements or in parts per million for trace elements. The results are presented in Table 2.

6.1. K-feldspar alteration

Typical K-feldspar altered rocks from both hanging wall and footwall of the main fault in Borehole 56-4 were selected for analysis, and they were compared with the igneous compositions of the Linglong granite in the isocon diagram (Fig. 10a).

The data show a decreasing trend of Na_2O and CaO and a large increase of K_2O, as expected from the replacement of plagioclase by K-feldspar. During the consumption of biotite, FeO and MgO are removed. The obvious loss of P_2O_5 mainly reflects the breakdown of P-rich accessory minerals (such as apatite and monazite).

LILEs exhibit high mobility during K-feldspar alteration. Rb and Pb are enriched due to their preference of substitution for K in the lattice of K-feldspar, whereas Sr and Ba are depleted, reflecting the breakdown of former Sr- and Ba-rich igneous feldspars (K-feldspar within the fresh granitic wall rocks can contains up to 2.90 wt.% BaO and 0.40 wt.% SrO, our unpublished data). The K-feldspar alteration is also characterized by a large gain of U, which is proven to be fluid mobile in many cases.

K-feldspar alteration is also accompanied by marked modifications of REEs concentrations and patterns. The total REEs contents of altered rocks are much lower than those of granitic wall rocks (Table 1). REEs are usually hosted in accessory zircon, apatite, titanite or monazite. Petrographic observation shows that with increasing alteration intensity the accessory minerals were gradually consumed.

Table 2
Calculated gains and losses for the different alteration zones.

	K-feldspar alteration	Sericitization	Silicification
SiO_2	1.69	3.24	41.83
TiO_2	−0.11	0.01	−0.10
FeO	−0.75	−0.45	1.04
MgO	−0.12	0.03	0.20
CaO	−0.55	0.80	−1.27
Na_2O	−1.57	−4.74	3.27
K_2O	3.80	1.19	−0.94
P_2O_5	−0.02	0.00	−0.02
LOI	0.26	3.07	−1.57
Sc	−0.44	−0.05	1.73
V	−3.05	−1.22	21.65
Cr	−61.20	−46.75	200.09
Co	−0.63	−0.31	1.04
Ni	−1.62	−0.56	5.43
Cu	1.15	11.44	129.81
Zn	−18.07	68.09	−77.93
Ga	2.49	−4.43	24.69
Rb	109.28	14.24	17.80
Sr	−284.62	−209.68	−206.65
Y	−3.12	−2.42	−1.31
Zr	−85.23	14.20	−70.64
Nb	−5.46	−4.44	−0.04
Cs	0.07	−0.50	0.05
Ba	−754.40	−37.15	−1178.66
La	−13.48	4.53	−17.42
Ce	−21.85	5.70	−27.53
Pr	−2.62	0.52	−3.16
Nd	−8.84	1.07	−10.56
Sm	−1.35	−0.26	−1.53
Eu	−0.12	0.21	−0.36
Gd	−0.93	−0.42	−0.90
Tb	−0.13	−0.08	−0.09
Dy	−0.52	−0.25	−0.38
Ho	−0.09	−0.03	−0.06
Er	−0.22	−0.06	−0.14
Tm	−0.04	−0.01	−0.02
Yb	−0.24	−0.04	−0.19
Lu	−0.04	0.00	−0.04
Hf	−2.07	0.37	−2.02
Ta	−0.26	−0.34	0.05
Pb	15.12	26.21	46.84
Bi	0.00	0.01	0.51
Th	0.68	0.02	−1.21
U	3.07	−0.75	1.32

This is also supported by the obvious depletion of P_2O_5, Ti and Zr (Table 1 and Fig. 10a). Therefore, the decrease of REE contents may be associated with the breakdown of REE-rich accessory minerals. It is also noted that there was much larger loss in LREEs (from La to Eu) than in HREEs (from Gd to Lu) (Fig. 10a and Table 2), indicating the higher mobility of LREEs during fluid–rock interactions, in conformity with similar observations in former studies (Guo et al., 2012; Küpeli, 2010; Panahi et al., 2000; Zhao et al., 2007).

Three altered K-feldspar samples (K-1995, K-2047, K-2048) display pronounced positive Eu anomalies (δEu = 8.46–14.67), and they are also characterized by very low total REE contents (1.19–2.68 ppm) (Fig. 11a). As mentioned above, along with the increased alteration intensity, relatively REE-rich minerals (e.g., monazite, zircon and apatite) gradually broke down. The major rock-forming minerals (e.g. K-feldspar and albite), which are commonly REE-poor, probably became the most important REE budget for the whole rock. In this case, the total REEs concentrations of altered rocks should be low, and the whole-rock chondrite-normalized REE patterns are similar to those of feldspar minerals, which have been shown to be very compatible with Eu by previous studies (Bédard, 2006; White, 2003).

Heavy chemical leaching of Nb, Ta, Zr and Hf is also observed. Zr and Hf tend to reside in zircon, and Nb and Ta are contained in titanium minerals (e.g., titanite and ilmenite). Losses of the HFSE should result from the consumption of related accessory minerals. Strong Zr–Hf, Nb–Ta and Y–Ho fractionations are observed in some altered samples, with deviations of Zr/Hf, Nb/Ta and Y/Ho values from corresponding magmatic ratios (Table 1). Ga displays much lower mobility than the other HFSE mentioned above. The ionic radii of Al and Ga are very similar that most of the Ga is present in Al-bearing minerals, and therefore Ga maintains similar immobility with Al.

6.2. Sericitization

Representative sericitization assemblages from both hanging wall and footwall of the main fault in Borehole 56-4 were analyzed, with the Linglong granite as their precursor.

Sericitization is characterized by strong gains of K_2O and LOI and loss of Na_2O, due to the replacement of plagioclase by sericite. CaO should also be lost in response to the consumption of plagioclase, but there is a gain of CaO shown in the isocon diagram (Fig. 10b), which may be caused by the presence of quartz-carbonate veinlets. As expected, the breakdown of biotite led to the depletion of FeO.

In the sericitization zone, Rb and Pb show gain due to their substitution of K in the lattice of sericite and K-feldspar. Sr was lost due to the consumption of igneous plagioclase, whereas Ba shows immobility, which is probably related to the conservation of K-feldspar during sericitization. U and Cs display slight to moderate loss.

During the sericitization stage, REEs and HFSEs show relatively lower mobility (Fig. 10b). LREEs (except for Sm) display minor gain, whereas Sm and HREEs show slight loss. The altered rocks display similar chondrite-normalized REE patterns with the Linglong granite (Fig. 11b). Most HFSEs were retained in the rocks, except for Nb and Ta which were moderately decreased. Zr–Hf, Nb–Ta and Y–Ho fractionations are also observed in sericitization domains (Table 1).

Some TRTEs (e.g. Cu, Zn and Bi) were largely enriched, probably resulting from the presence of disseminated sulfide.

6.3. Silicification

Typical silicification assemblages were analyzed from the hanging wall of the Borehole 56-4. As mentioned above, silicification overprinted earlier sericitization, so gains and losses of elements are tested by plotting average element concentrations of altered rocks in the silicification zone versus those in sericitization zone in the isocon diagram (Fig. 10c).

Silicification is characterized by a strong addition of SiO_2 and losses of K_2O, CaO, P_2O_5 and LOI, resulting from the fact that quartz replaced the former igneous and secondary minerals. Na_2O shows increase, which contradicts the consumption of plagioclase. Considering that there are many fluid inclusions within the secondary quartz, we infer that the Na_2O reside in fluid inclusions in quartz. FeO also shows gain, due to the presence of disseminated pyrite.

Along with the consumption of former K-feldspar, plagioclase and sericite, Sr and Ba were lost. Pb and U were gained, which may also be related to the common presence of fluid inclusions within the secondary quartz. Compared with the LILEs mentioned above, Rb and Cs show very slight mobility (Fig. 10c).

As with K-feldspar alteration, all the REEs were lost from former altered rocks, and the LREEs generally display higher mobility than the HREE (Fig. 10c and Table 2). The chondrite-normalized REE patterns were changed: two analyzed samples have low total REE contents (7.80–10.18 ppm) and moderately positive Eu anomalies (Fig. 11a). This might also have resulted from the marked consumption of REE-rich accessory minerals and presence of feldspars in silicification zone.

The behavior of HFSEs is complex in the silicification zone. Zr, Hf, Ti and Th were moderately to largely lost, whereas Ga shows large enrichment. Nb and Ta show minor mobility. The Nb/Ta, Zr/Hf and Y/Ho values deviate from those of the Linglong granite (Table 1).

Silicification is also marked by addition of most TRTEs (e.g. Sc, V, Cr, Co, Ni and Cu) due to the precipitation of sulfide.

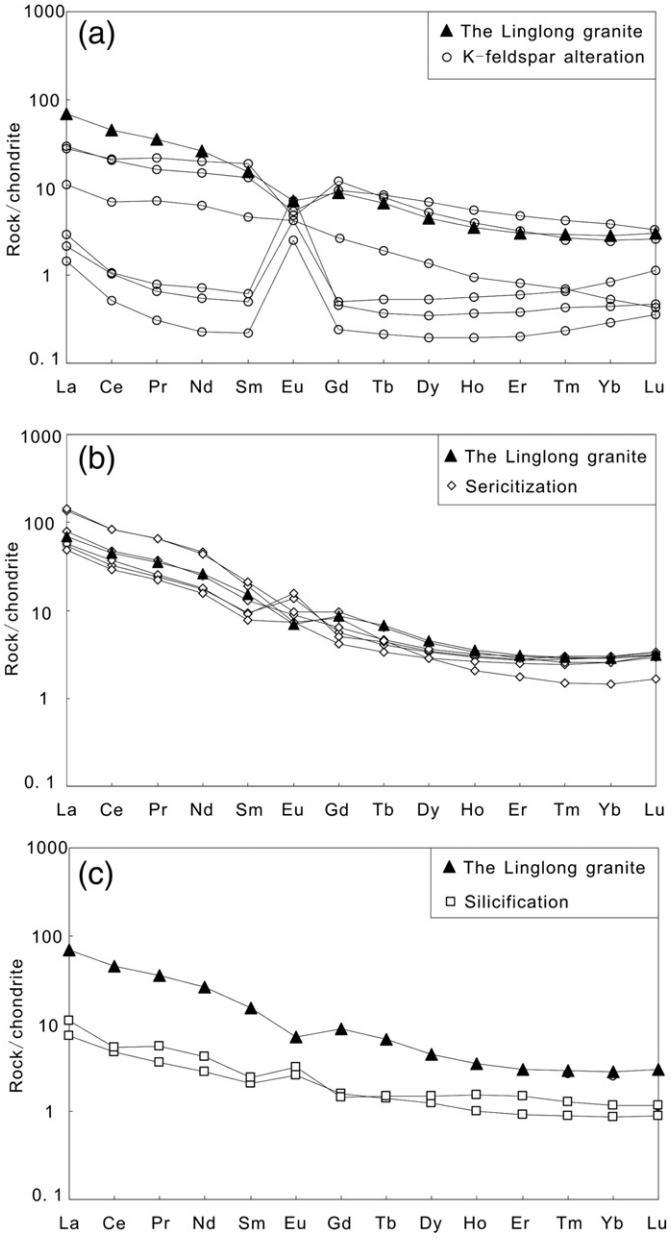

Fig. 11. Chondrite-normalized REE patterns for sample undergone K-feldspar alteration (a), silicification (b) and sericitization (c). Chondrite-normalized REE pattern for the Linglong granite is also shown for comparison. The chondrite values are from Sun and McDonough (1989).

6.4. Pyrite–sericite–quartz alteration

For rocks in the pyrite–sericite–quartz alteration zone, it is inevitable to include some samples with a few veins/stockworks. In addition, pyrite–sericite–quartz alteration may have overprinted either sericitization or silicification, so it is hard to define the "protoliths" of pyrite–sericite–quartz alteration. Therefore, we presented only the whole-rock major and trace element data for pyrite–sericite–quartz altered rocks in Table 1, and do not attempt to compare them with any precursors.

Due to the common presence of sulfide minerals, which are spatially close to gold as mentioned above, this zone is characterized by obvious addition of S and Au. Along with the addition of gold, other metal elements (e.g. Cu, Pb and Bi) are also enriched (Table 1). Former studies found that at relatively lower temperatures (<400 °C), HS^- is the most important ligand complexed with gold (Seward, 1973), with $Au(HS)^0$ predominating at acidic condition and $Au(HS)_2^-$ at weakly acidic to neutral conditions (Stefánsson and Seward, 2004); whereas at a high temperature, high salinity and H_2S-poor systems, $AuCl^{2-}$ will predominate (Mikucki, 1998; Stefánsson and Seward, 2004). The close association of gold with sulfides in the pyrite–sericite–quartz alteration zone supports that gold was most likely complexed with HS^- during transportation.

6.5. Summary

The presence of large mineralized bodies, wide alteration halos and strong modification of igneous textures and mineral assemblages indicate large scale and intense fluid–rock interaction. Such hydrothermal processes should have the potential to mobilize most elements when fluids fluxed through granitic wall rocks.

As shown in the previous section, major element concentrations are affected by various mineral replacement reactions. Most fluid-mobile elements, LILEs and LREEs, show relatively high mobility. The traditionally assumed fluid-immobile elements (e.g. HREEs and HFSEs) could also be changed, especially during the K-feldspar alteration and silicification stages. In fact, mobilization of HREEs and HFSEs owing to hydrothermal alteration has been reported by several authors (e.g. Dongen et al., 2010; Hynes, 1980; Jiang, 2000; Jiang et al., 2005; Salvi and Williams-Jones, 1996; Salvi et al., 2000). These observations are noteworthy because these elements, especially the REEs and HFSEs, are widely used for petrogenetic studies; therefore, caution must be taken with samples which are hydrothermally altered.

7. Physicochemical conditions of ore fluid system

In this section, previous fluid inclusion data and newly computed log (a_K^+/a_H^+)-log (a_{Na}^+/a_H^+) and logf_{O2}-pH diagrams are employed to derive the principal physicochemical parameters (e.g. temperature, pressure, pH, f_{O2} and fluid compositions) that potentially controlled the hydrothermal alteration and gold mineralization.

Coexistence of ductile deformation of quartz and slight brittle deformation of the feldspar in the altered rocks (Figs. 4e and 5f) indicates that deformation, and thus gold mineralization, occurred under temperature conditions of 300–400 °C (Scholz, 1988). As mentioned above, rocks adjacent to the main fault underwent strong brittle deformation (Figs. 6c, 7a and b), and before that quartz in the alteration halos had experienced slight to moderate ductile deformation. These facts suggest that the Sanshandao–Cangshang fault is a brittle-ductile transitional deformation zone, but it is dominantly characterized by cataclastic deformation. Therefore, it is deduced that the deformation occurred at depth of about 10 km (Sibson, 1977), corresponding to pressure of about 300 MPa. The deduced temperature and pressure are broadly consistent with those obtained by Fan et al. (2003) from fluid inclusions in mineralizing stage. Therefore, we chose 350 °C and 300 MPa for phase equilibria calculations.

Stability relationships of Na–K alteration phases were determined as a function of fluid composition and an isothermal–isobaric abridged activity diagram [log (a_K^+/a_H^+) versus log (a_{Na}^+/a_H^+)] was constructed in the system Na–K–Al–Si–H–O (Fig. 12a). The phases considered are K-feldspar ($KAlSi_3O_8$), albite ($NaAlSi_3O_8$), sericite [$KAl_2(AlSi_3)O_{10}(OH)_2$], paragonite [$NaAl_2(AlSi_3)O_{10}(OH)_2$] and kaolinite [$Al_2Si_2O_5(OH)_4$]. End-member reactions used for the construction of the log (a_K^+/a_H^+) versus log (a_{Na}^+/a_H^+) diagram and the computed log K values are given in Table 3 (A1–A7). Log f_{O2}-pH diagram for the system Fe–S–O–H was also constructed to depict phase relationships of Fe-bearing minerals and fields of predominance of aqueous sulfur species (Fig. 12b). The species boundaries between H_2S, HS^-, HSO_4^- and SO_4^{2-} were determined using log K values of A8 through A12 (Table 3). Mineral stability fields were plotted based on log K values of A13 through A19 (Table 3). The concentration of total dissolved sulfur in solution was on the order of

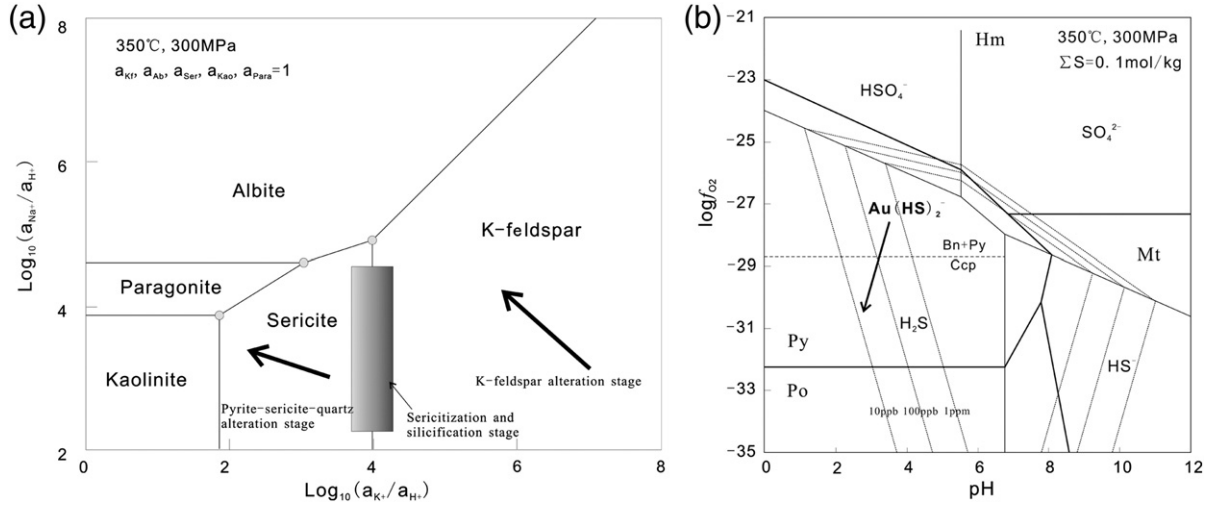

Fig. 12. (a) log (a_K^+/a_H^+)-log (a_{Na}^+-a_H^+) diagram at 350 °C and 300 MPa. Note that fluids evolved to lower log (a_K^+/a_H^+) with alteration going on (thermodynamic data used are from slop98.dat database). (b) Log f_{O2}-pH diagram at 350 °C, 300 MPa and ΣS = 0.1 mol/kg (the thermodynamic properties for $Au(HS)_2^-$ are from Akinfiev and Zotov (2010); other data are from the slop98.dat database). Narrow and bold lines, represent the boundaries between aqueous sulfur species and Fe-bearing minerals, respectively. Calculated solubility contours of $Au(HS)_2^-$ at 10, 100 and 1000 ppb (thin continuous lines) are shown in the predominance fields of various aqueous sulfur species. The arrow represents the possible decrease of f_{O2}, with marginal drop in pH, caused gold precipitation. Abbreviations: Hm—hematite, Mt—magnetite, Py—pyrite, Po—pyrrhotite, Bn—bornite, Ccp—chalcopyrite.

ΣS = 0.1 mol/kg, which is within the ΣS range ($10–10^{-3.5}$ mol/kg) compiled by Mikucki (1998) for the orogenic gold deposits.

In K-feldspar alteration stage, replacement of plagioclase by K-feldspar could lead to a decrease of a_K^+ and an increase of a_{Na}^+ in aqueous solutions, and the fluid compositions locate in the stability field of K-feldspar in log (a_K^+/a_H^+)-log (a_{Na}^+/a_H^+) diagram (Fig. 12a). During sericitization and silicification stages, plagioclase was transformed into sericite, but K-feldspar experienced little alteration. Thus, log (a_K^+/a_H^+) of the fluid is constrained on the equilibrium line between K-feldspar and sericite (Fig. 12a). Pyrite–sericite–quartz alteration is marked by the common presence of sericite and disappearance of both plagioclase and K-feldspar, so the fluid compositions should be confined in the stability field of sericite, and the formation of sericite would lead to a decrease of a_K^+ in the fluid (Fig. 12a). In general, the hydrothermal fluids were marked by decreases of log (a_K^+/a_H^+) from early to late alteration stages, which can be caused by a decrease of a_K^+ and/or an increase of a_H^+.a_H^+ generally kept constant due to weak acid buffering by H_2CO_3 utilizing the common presence of CO_2 in the fluid (Phillips and Evans, 2004), but formation of secondary K-feldspar and sericite would largely consume K^+ in the fluid. Thus, decrease of a_K^+ was probably responsible for the decreases of log (a_K^+/a_H^+) of the fluids.

In relatively acid solutions, feldspar tends to be transformed into sericite (Sverjensky et al., 1991; A2 and A3 in Table 3). However, sericite is not stable if the acidity is strong, under which sericite can be replaced by kaolinite (Sverjensky et al., 1991; A4 in Table 3). Therefore, the common presence of sericite in ore-bodies can be effectively used to constrain pH of ore-forming fluids. If activity coefficients are ignored (γ = 1), temperature was 350 °C, pressure was 300 MPa, sodium ion concentrations of the fluid were assumed to be 1 mol/kg (~6 wt.% NaCl equiv) based on the calculated salinities of fluid inclusions and the potassium concentration was assumed to be 0.1 m/kg, which corresponds to a Na/K ratio of 10, an estimate that is similar to that of other mesothermal gold deposits (Diamond et al., 1991; Robert and Kelly, 1987; Yardley, 2005), pH is calculated to be between 2.9 and 5.0 in order for sericite to be stable. This is consistent with the weak acidity suggested by the presence of CO_2 in the mineralizing fluids.

f_{O2} of ore-forming fluid can be constrained based on the phase relationships of Fe-bearing minerals in Fig. 12b. Pyrite is the predominant Fe-bearing mineral in ore-bodies, which assigns log f_{O2} between −25.08 and −32.22, assuming pH = 4, T = 350 °C and P = 300 MPa. In addition, chalcopyrite is the most important accessory sulfide mineral, which usually coexists with pyrite (Fig. 7f). The coexistence of these minerals during the main mineralizing stage further constrains log f_{O2} near −28 (Fig. 12b). This paper does not cover fluid inclusion studies for specimen from deep boreholes, but it is notable that through fluid inclusion studies Fan et al. (2003) found that CH_4 was almost absent in the fluids of pre-gold alteration stages, whereas it was commonly present in fluid inclusions in the main gold mineralization stage at Sanshandao. This might indicate a decrease of f_{O2} from pre-metallogenic stage to the main gold

Table 3
Reactions with their LogK values used to construct Fig. 12 (thermodynamic properties for $Au(HS)_2^-$ are from Akinfiev and Zotov (2010); all other data are from the slop98.dat database). Note: aq represents aqueous phase; g denotes gas phase.

Reaction no.	Reaction	LogK
A1	$Na(AlSi_3)O_8 + K^+ = K(AlSi_3)O_8 + Na^+$	0.929
A2	$3K(AlSi_3)O_8 + 2H^+ = KAl_2(AlSi_3)O_{10}(OH)_2 + 6SiO_2 + 2K^+$	7.951
A3	$3Na(AlSi_3)O_8 + 2H^+ + K^+ = KAl_2(AlSi_3)O_{10}(OH)_2 + 6SiO_2 + 3Na^+$	10.739
A4	$2KAl_2(AlSi_3)O_{10}(OH)_2 + 2H^+ + 3H_2O = 3Al_2Si_2O_5(OH)_4 + 2K^+$	3.705
A5	$KAl_2(AlSi_3)O_{10}(OH)_2 + Na^+ = NaAl_2(AlSi_3)O_{10}(OH)_2 + K^+$	−1.511
A6	$3Na(AlSi_3)O_8 + 2H^+ = NaAl_2(AlSi_3)O_{10}(OH)_2 + 6SiO_2 + 2Na^+$	9.228
A7	$2NaAl_2(AlSi_3)O_{10}(OH)_2 + 2H^+ + 3H_2O = 3Al_2Si_2O_5(OH)_4 + 2Na^+$	6.727
A8	$H_2S,aq = HS^- + H^+$	−6.768
A9	$HSO_4^- = SO_4^{2-} + H^+$	−5.511
A10	$HS^- + 2O_2,g = SO_4^{2-} + H^+$	49.204
A11	$H_2S,aq + 2O_2,g = HSO_4^- + H^+$	47.947
A12	$H_2S,aq + 2O_2,g = SO_4^{2-} + 2H^+$	42.436
A13	$2FeS + O_2,g + 2H_2S,aq = 2FeS_2 + 2H_20,aq$	34.218
A14	$2FeS + O_2,g + 2HS^- + 2H^+ = 2FeS_2 + 2H_20,aq$	47.754
A15	$6FeS + 6H_2O,aq + O_2,g = 2Fe_3O_4 + 6HS^- + 6H^+$	−22.634
A16	$3FeS_2 + 6H_2O,aq = Fe_3O_4 + 6HS^- + 6H^+ + O_2,g$	−82.947
A17	$3FeS_2 + 6H_2O,aq + 11O_2,g = Fe_3O_4 + 6SO_4^{2-} + 12H^+$	212.276
A18	$4FeS_2 + 8H_2O,aq + 15O_2,g = 2Fe_2O_3 + 8SO_4^{2-} + 16H^+$	292.138
A19	$4FeS_2 + 8H_2O,aq + 15O_2,g = 2Fe_2O_3 + 8HSO_4^- + 8H^+$	336.226
A20	$4Au + 8H_2S,aq + O_2,g = 4Au(HS)_2^- + 2H_2O,aq + H^+$	−3.936
A21	$4Au + 8HS^- + O_2,g + 4H^+ = 4Au(HS)_2^- + 2H_2O,aq$	50.204
A22	$4Au + 8SO_4^{2-} + 12H^+ = 4Au(HS)_2^- + 2H_2O,aq + 15O_2,g$	−343.424
A23	$4Au + 8HSO_4^- + 4H^+ = 4Au(HS)_2^- + 2H_2O,aq + 15O_2,g$	−387.512

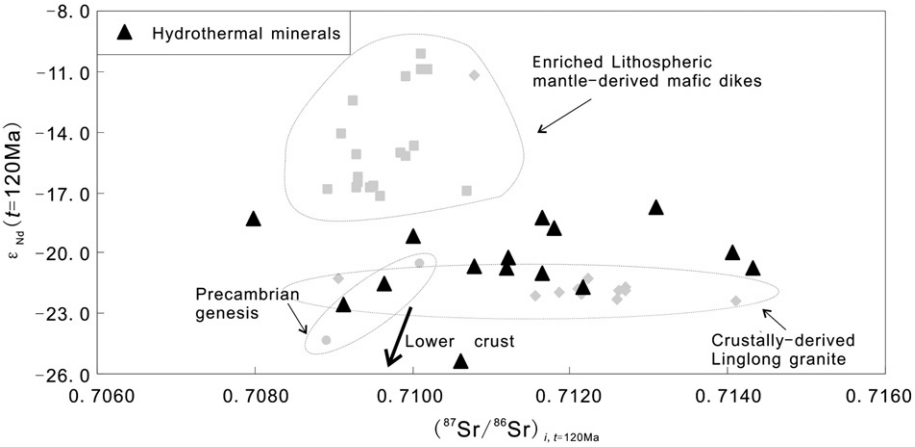

Fig. 13. Isotopic compositions of Sr and Nd for hydrothermal minerals from the Sanshandao gold deposit. Published compositional fields for Early Cretaceous mantle-derived mafic dikes (Yang et al., 2004), the Jurassic crustally-derived Linglong granite from the Jiaobei terrane (Hou et al., 2007; Zhang et al., 2010), Precambrian genesis in the upper crust (Yang and Zhou, 2001) and trend to lower crust (Jahn et al., 1999) are also shown for comparison.

metallogenic stage, at least locally in the Sanshandao deposit itself. If this is a common process in the whole gold-forming belt needs further systematic study.

As mentioned above, the ore-forming fluid in mineralizing stage was characterized by moderate temperature, low salinity and weak acidity. This, combined with the close association of gold with sulfides in ore bodies, suggests that gold was most likely transported as a gold bisulfide complex (Mikucki, 1998; Stefánsson and Seward, 2004; Williams-Jones et al., 2009).

Contours of $Au(HS)_2^-$ concentration were calculated as a proxy for gold solubility using the reactions A20 through A23 (Table 3). The nature of the solubility contours of $Au(HS)_2^-$ in the H_2S predominance field (Fig. 12b) is of particular interest because the predominance field of H_2S generally overlap with the stability field of pyrite. Solubility of gold in the H_2S predominance field is controlled by the following reaction:

$$Au + 2H_2S, aq + 0.25O_2, g = Au(HS)_2^- + 0.5H_2O + H^+.$$

Applying Le Châtelier's principle, we can therefore predict that gold precipitation could be enhanced by a decrease in f_{O2} and/or pH. However, since dramatic pH change should be resisted by the abundant CO_2 in solutions, a decrease in f_{O2} might be more effective for gold precipitation. As mentioned above, the significant presence of CH_4 in gold-bearing fluids of the Sanshandao deposit may suggest that there was a decrease in f_{O2} during mineralization, so it is deduced that decrease of f_{O2} was probably one of the factors controlling the precipitation of gold in the Sanshandao deposit.

8. Possible sources of ore fluids

Characteristics of mineralization, alteration and ore fluids suggest that the Sanshandao gold deposit shares many features of orogenic gold deposits hosted in Precambrian cratons worldwide (Goldfarb et al., 2001, 2005; Groves et al., 1998; Kerrich and Cassidy, 1994). These deposits formed mostly in the time intervals of 2.8 to 2.55 and 2.1 to 1.8 Ga in compressional to transpressional tectonic regimes coupled with metamorphism during craton stabilization. However, regional metamorphism in the eastern North China Craton took place in the Late Archean to early Paleoproterozoic (Zhai and Santosh, 2011; Zhao et al., 2005, and references therein), billions of years prior to the Early Cretaceous gold mineralization. Thus, regional metamorphic fluid component is regarded as minimal for the mineralization of the Sanshandao deposit.

Previous studies on H–O isotopes of the Sanshandao gold deposits showed that oxygen isotope ratios for auriferous quartz samples range from 9.7 to 13.7‰, with the calculated ore-fluid $\delta^{18}O$ values being 6.6 to 10.9‰, and the hydrogen isotopes measured for inclusion fluids extracted from auriferous quartz range from −48 to −81‰ (Fan et al., 2003; Mao et al., 2008). These data locate within or adjacent to the magmatic water region in the plot of δD vs. $\delta^{18}O$, suggesting that a magmatic fluid might have dominated at the Sanshandao deposit. Nevertheless, the ore fluids may also contain a portion of meteoric waters, as some δD values are lighter than typical values of primary magmatic waters. Furthermore, typical exsolved magmatic fluid is characterized by high temperatures and relatively high salinity (Audétat et al., 2008), so external, largely meteoric, fluids were needed to mix with the magmatic fluid to produce the moderate-temperature and low salinity ore-forming fluids as suggested by fluid inclusions in the Sanshandao deposit. This lends additional support for the involvement of meteoric water in the ore-forming system.

It is possible that during fluid generation and migration, Sr and Nd entered the ore fluids, and during large scale and intense fluid–rock interactions, the isotopic signature of the fluids was recorded in the newly formed hydrothermal minerals. Investigations by Bell et al. (1989), Frei et al. (1998) and Yang and Zhou (2001) have shown that the sources of hydrothermal fluids can be determined by Rb–Sr, and Sm–Nd isotopic studies of hydrothermal minerals. In this paper, the isotopic data of the hydrothermal minerals (secondary K-feldspar, sericite and pyrite) from alteration and mineralization zone are employed to provide further constraints on the source of the hydrothermal fluids.

The ε_{Nd} values of hydrothermal minerals at 120 Ma are within the range −17.7 to −25.2, and the initial $^{87}Sr/^{86}Sr$ ratios at 120 Ma range from 0.7088 to 0.7143, with most values higher than 0.7110 (Fig. 13 and Table 4). Previous studies yielded similar Sr [$(^{87}Sr/^{86}Sr)_{i=117\ Ma}$: 0.7103 to 0.7119] and Nd [$\varepsilon_{Nd}(t=117Ma)$: −16.1 to −20.0] isotopic compositions for mineralized rocks in the Xincheng gold deposit, another large Jiaojia-type deposit near the Sanshandao gold deposit (Yang, 2000). The high initial $^{87}Sr/^{86}Sr$ ratios of hydrothermal minerals generally overlap with those of crustally-derived granitoids (Fig. 13), which suggests that Sr in the mineralizing fluids was mainly derived from a crustal source. The low diffusion rate of Nd isotope in minerals (Cherniak, 2003; Michard, 1989) suggests that there might be limited fluid–wall rock Nd isotopic exchange during fluid migration and thus, Nd isotopic composition can largely reflect the nature of the fluid source. The strongly negative ε_{Nd} (t) values for hydrothermal minerals suggest that Nd isotopic composition of the hydrothermal fluids mainly derived from crustal source. Early Cretaceous granitoids contemporaneous with the gold deposits crop out widely in the Jiaobei terrane, which indicate widespread crust reactivation and melting (Zhai, 2008). Post-magmatic fluids of felsic magmas may have easily ascended along a regional fault and largely participated in the gold-forming event. In

Table 4
Sr and Nd isotopic compositions for hydrothermal minerals. Note: Chondrite Uniform Reservoir (CHUR) values ($^{87}Rb/^{86}Sr = 0.0847$, $^{87}Sr/^{86}Sr = 0.7045$, $^{147}Sm/^{144}Nd = 0.1967$, $^{143}Nd/144Nd = 0.512638$) are used for the calculation. $\lambda_{Rb} = 1.42 \times 10^{-11}$ year^{-1}, $\lambda_{Sm} = 6.54 \times 10^{-12}$ year^{-1} (Lugmair and Harti, 1978).

Sample no.	Rb (ppm)	Sr (ppm)	$^{87}Rb/^{86}Sr$	$^{87}Sr/^{86}Sr$	$(^{87}Sr/^{86}Sr)_i$	$\pm 2\sigma$	Sm (ppm)	Nd (ppm)	$^{147}Sm/^{144}Nd$	$^{143}Nd/^{144}Nd$	$\varepsilon_{Nd}(0)$	$\varepsilon_{Nd}(t)$	$\pm 2\sigma$
Secondary													
K-feldspar													
1800-kf	276.35	372.87	2.15	0.715305	0.711706	0.000013	0.02	0.08	0.11	0.511639	−19.5	−18.2	0.0009
1862-kf	322.31	120.81	7.73	0.726280	0.713311	0.000011	0.11	0.42	0.16	0.511699	−18.3	−17.7	0.0009
1995-kf	287.56	298.77	2.79	0.715965	0.711291	0.000012	0.00	0.02	0.13	0.511548	−21.3	−20.2	0.0011
2036-kf	96.77	863.70	0.32	0.712200	0.711656	0.000016	0.18	1.30	0.08	0.511471	−22.8	−21.0	0.0007
2048-kf	235.28	386.35	1.76	0.714794	0.711837	0.000012	0.03	0.16	0.10	0.5116	−20.2	−18.7	0.0008
Sericite													
1967-ser	264.62	11.72	61.76	0.814965	0.711390	0.000009	1.59	9.99	0.10	0.511458	−23.0	−21.5	0.0011
1975-ser	268.09	33.58	21.68	0.749138	0.712775	0.000019	1.68	11.09	0.09	0.511446	−23.3	−21.7	0.0010
2020-ser	262.86	40.22	19.25	0.741958	0.709668	0.000009	1.36	9.89	0.08	0.511392	−24.3	−22.6	0.0009
2047-ser	274.91	33.08	21.44	0.747214	0.711255	0.000011	0.92	7.40	0.08	0.511251	−27.1	−25.2	0.0019
2047b-ser	334.01	33.58	28.92	0.757318	0.708818	0.000014	0.94	5.65	0.10	0.511625	−19.8	−18.3	0.0007
1884-ser	337.53	12.31	80.40	0.847085	0.712250	0.000008	0.77	4.11	0.11	0.511597	−20.3	−19.0	0.0010
Pyrite													
1960-py	2.06	1.29	4.62	0.718656	0.710908	0.000015	0.04	0.27	0.10	0.511505	−22.1	−20.6	0.0014
1962-py	0.59	1.33	1.29	0.713395	0.711236	0.000015	0.05	0.31	0.10	0.511497	−22.3	−20.7	0.0009
1963-py	0.09	2.21	0.12	0.714511	0.714313	0.000016	0.04	0.21	0.11	0.511505	−22.1	−20.7	0.0009
1976-py	0.57	1.13	1.45	0.716522	0.714095	0.000020	0.02	0.12	0.11	0.511546	−21.3	−20.0	0.0010

addition, meteoric water which had equilibrated with crustal rocks can also be induced by widespread intrusions to participate in the ore-forming event. It should also be noted that some $\varepsilon_{Nd}(t)$ values of hydrothermal minerals are relatively higher than published crustal values for the North China Craton (Jahn et al., 1999) and those of the crustally-derived granitic wall rocks, but can be compared with those of mafic dikes (Fig. 13), which suggests the possibility that fluids derived from an enriched lithospheric mantle might have also participated in the ore-forming process. Given the close spatial and temporal relationship between gold deposits and the 122–124 Ma mafic dikes, the fluid degassed from parental magma of mafic dikes most likely contributed to the ore-forming fluids. Previous He–Ar isotopic studies on representative Jiaodong gold deposits also recognized the trace of mantle derived fluids are involved in the gold mineralization event (Zhang et al., 2008). In general, the Sr and Nd isotopic compositions of hydrothermal minerals indicate that the ore fluids for the Sanshandao deposit were mainly derived from crustal sources, but coupled with the addition of mantle-derived components.

One of the most important observations on the NCC resulting from various studies in the last few decades is that the lithosphere of this craton was considerably modified during the Phanerozoic, where the cold and thick cratonic lithosphere (~200 km) in the Paleozoic was replaced by a hot and thin "oceanic" one (<80 km) (Griffin et al., 1998). During this process, the stability of the coupled lithospheric mantle and crust was affected, leading to lithospheric mantle thinning and refertilization as well as crustal activation (Li et al., 2013; Zhai, 2008). In Early Cretaceous, mafic to felsic magmatism are widely recognized in the eastern North China Craton, and their genesis has been commonly interpreted as crustal–mantle interactions (Chen et al., 2008; Qian and Hermann, 2010; Xu et al., 2004; Zhang et al., 2013). The presence of metamorphic core complexes (Davis et al., 2001; Liu et al., 2005), formation of NE-striking half-graben basins (Ren et al., 2002; Tian et al., 1992) and activation of large scale strike-slip fault (Tan–Lu fault) (Zhu et al., 2001) indicate an extensional geodynamic setting. It is conceivable that voluminous magmas from different sources, induced by asthenosphere upwelling and crust reactivation, could have provided heat and fluid input contributing to the large-scale gold mineralization. In addition, asthenospheric upwelling and strong crust–mantle interactions within a thinned lithosphere led to high crustal heat flow, which could induce voluminous meteoric fluid flow to participate in the ore-forming process. Extensional structures were formed in the upper crust, providing flow channels and sites for gold precipitation.

Collectively, stable, radiogenic and noble gas isotope compositions are consistent with multiple sources of the ore-forming fluids in the Sanshandao deposit. Crustally-derived fluids (degassing of felsic magmas and meteoric water) may constitute a major portion of the ore fluids, but mantle derived fluids, most probably degassing of the parental magmas which generated the mafic dikes, were also involved in gold mineralization. This is in accord with the regional background of strong crust–mantle interactions in the Early Cretaceous.

9. Conclusion

Intense fluid–rock interaction, over a zone of hundreds of meters around the regional Sanshandao–Cangshang fault zone, is a typical feature of the Sanshandao gold deposit. Relatively early K-feldspar alteration, sericitization and silicification were generally symmetrically developed on both hanging wall and footwall of the fault. The subsequent formed layer of fault gouge function as an impermeable horizon for the later fertile ore-forming fluid to move upward and thus, the intense pyrite–sericite–quartz alteration and related gold mineralization developed only in the footwall of the main fault. Finally, gold related fluid activity waned, as represented by the late quartz-carbonate veins.

Although the hydrothermal fluids were characterized by moderate temperature, low to moderate salinity and weak acidity, they still had the potential to mobilize most elements, including the commonly assumed fluid-immobile HREE and HFSE, during intense fluid–rock interactions. With alteration going on, $\log(a_K^+/a_H^+)$ of fluids generally decreased due to the formation of secondary K-bearing minerals, and there might be a decrease of f_{O2} from pre-gold alteration stage to the main gold mineralization stage. Gold, most likely transported as $Au(HS)_2^-$ complex, was probably deposited in response to f_{O2} decrease of the ore-forming fluids.

Sr–Nd isotopes of hydrothermal minerals and H–O and He–Ar data of ore fluids, combined with the regional background of strong crust–mantle interaction, favor a mixed source of the ore-forming fluids. Although crustally-derived magmatic and meteoric water constitute the dominant portion of the ore fluids, the signature of mantle-derived fluids was also identified to participate in the gold mineralization. The gold metallogeny occurred within the tectonic framework of lithosphere thinning and reactivation of the North China Craton, which not only provided the heat and fluid input, but also generated favorable structural sites for fluid flow and gold deposition.

Acknowledgment

Dr. Richen Zhong from Peking University is greatly appreciated for his assistance with the phase equilibrium calculation by means of SUPCRT92 software. Sincere thanks are extended to Xiannian Jin from the Shandong Gold Group Co. Ltd. for his helps during the fieldwork. Two anonymous referees and the editor Dr. Olga Plotinskaya are thanked for their constructive and valuable comments which greatly contributed to the improvement of the manuscript. This study was financially supported by the Natural Science Foundation of China (41173056), 100 Talents Programme of the Chinese Academy of Sciences and the Crisis Mines Continued Resources Exploration Project of China Geological Survey (20089930).

References

Akinfiev, N.N., Zotov, A.V., 2010. Thermodynamic description of aqueous species in the system Cu–Ag–Au–S–O–H at temperatures of 0–600 °C and pressures of 1–3000 bar. Geochem. Int. 48, 714–720.

Audétat, A., Pettke, T., Heinrich, C.A., Bodnar, R.J., 2008. The composition of magmatic-hydrothermal fluids in barren and mineralized intrusions. Econ. Geol. 103, 877–908.

Bédard, J.H., 2006. Trace element partitioning in plagioclase feldspar. Geochim. Cosmochim. Acta 70, 3717–3742.

Bell, K., Anglin, C.D., Franklin, J.M., 1989. Sm–Nd and Rb–Sr isotope systematics of scheelites: possible implications for the age and genesis of vein-hosted gold deposits. Geology 17, 500–504.

Chen, G.Y., Shao, W., Sun, D.S., 1989. Genetic Mineralogy of Gold Deposits in Jiaodong Region with Emphasis on Gold Prospecting. Chongqing Publishing House, Chongqing (in Chinese).

Chen, Y.J., Pirajno, F., Qi, J.P., 2005. Origin of gold metallogeny and sources of ore-forming fluids, Jiaodong Province, Eastern China. Int. Geol. Rev. 47, 530–549.

Chen, B., Tian, W., Jahn, B.M., Chen, Z.C., 2008. Zircon SHRIMP U–Pb ages and in-situ Hf isotopic analysis for the Mesozoic intrusions in South Taihang, North China Craton: evidence for hybridization between mantle derived magmas and crustal components. Lithos 102, 118–137.

Cherniak, D.J., 2003. REE diffusion in feldspar. Chem. Geol. 193, 25–41.

Chu, Z.Y., Chen, F.K., Yang, Y.H., Guo, J.H., 2009. Precise determination of Sm, Nd concentrations and Nd isotopic compositions at the nanogram level in geological samples by thermal ionization mass spectrometry. J. Anal. At. Spectrom. 24, 1534–1544.

Davis, G.A., Zheng, Y.D., Wang, C., Darby, B.J., Zhang, C.H., Gehrels, G., 2001. Mesozoic tectonic evolution of the Yanshan fold and thrust belt, with emphasis on Hebei and Liaoning Provinces northern China. Geol. Soc. Am. Mem. 194, 171–198.

Diamond, L.W., Jackman, J.A., Charoy, B., 1991. Cation ratios of fluid inclusions in a gold-quartz vein at Brusson, Vald'Ayas, northwestern Italian Alps: comparison of bulk crush-leach results with SIMS analyses of individual inclusions. Chem. Geol. 90, 71–78.

Dongen, M., Weinberg, R.F., Tomkins, A.G., 2010. REE-Y, Ti, and P remobilization in magmatic rocks by hydrothermal alteration during Cu–Au deposit formation. Econ. Geol. 105, 763–776.

Fan, W.M., Guo, F., Wang, Y.J., Lin, G., Zhang, M., 2001. Post-orogenic bimodal volcanism along the Sulu Orogenic Belt in eastern China. Phys. Chem. Earth Solid Earth Geod. 26, 733–746.

Fan, H.R., Zhai, M.G., Xie, Y.H., Yang, J.H., 2003. Ore-forming fluids associated with granite-hosted gold mineralization at the Sanshandao deposit, Jiaodong gold province, China. Miner. Deposita 38, 739–750.

Fan, H.R., Hu, F.F., Yang, J.H., Shen, K., Zhai, M.G., 2005. Fluid evolution and large-scale gold metallogeny during Mesozoic tectonic transition in the eastern Shandong province. Acta Petrol. Sin. 21, 1317–1328 (in Chinese with English abstract).

Frei, R., Nagler, T.F., Schonberg, R., Kramers, J.D., 1998. Re–Os, Sm–Nd, U–Pb, and stepwise lead leaching isotope systematics in shear-zone hosted gold mineralization: genetic tracing and age constraints of crustal hydrothermal activity. Geochim. Cosmochim. Acta 62, 1925–1936.

Goldfarb, R.J., Groves, D.I., Gardoll, S., 2001. Orogenic gold and geologic time: a global synthesis. Ore Geol. Rev. 18, 1–75.

Goldfarb, R.J., Baker, T., Dube, B., Groves, D.I., Hart, C.J.R., Gosselin, P., 2005. Distribution, character, and genesis of gold deposits in metamorphic terranes. Econ. Geol. 407–450 (100th Anniversary volume).

Goldfarb, R.J., Hart, C., Davis, G., Groves, D., 2007. East Asian gold: deciphering the anomaly of phanerozoic gold in Precambrian cratons. Econ. Geol. 102, 341–345.

Goss, S.C., Wilde, S.A., Wu, F.Y., Yang, J.H., 2010. The age, isotopic signature and significance of the youngest Mesozoic granitoids in the Jiaodong Terrane, Shandong Province, North China Craton. Lithos 120, 309–326.

Grant, J.A., 1986. The isocon diagram—a simple solution to Gresens equation for metasomatic alteration. Econ. Geol. 81, 1976–1982.

Griffin, W.L., Zhang, A.D., O'Reilly, S.Y., Ryan, C.G., 1998. Phanerozoic evolution of the lithosphere beneath the Sino–Korean Craton. In: Flower, M.F.J., Chung, S.L., Lo, C.H., Lee, T.Y. (Eds.), Mantle Dynamics and Plate Interactions in East Asia. Geodynamic Series. American Geophysical Union, Washington, D.C., pp. 107–126.

Groves, D.I., Goldfarb, R.J., Gebre-Mariam, M., Hagemann, S.G., Robert, F., 1998. Orogenic gold deposits: a proposed classification in the context of their crustal distribution and relationship to other gold deposit types. Ore Geol. Rev. 13, 7–27.

Guo, S., Ye, K., Chen, Y., Liu, J.B., Mao, Q., Ma, Y.G., 2012. Fluid–rock interaction and element mobilization in UHP metabasalt: constraints from an omphacite–epidote vein and host eclogites in the Dabie orogen. Lithos 136–139, 145–167.

Hou, M.L., Jiang, Y.H., Jiang, S.Y., Ling, H.F., Zhao, K.D., 2007. Contrasting origins of late Mesozoic adakitic granitoids from the northwestern Jiaodong Peninsula, east China: implications for crustal thickening to delamination. Geol. Mag. 144, 619–631.

Hynes, A., 1980. Carbonatization and mobility of Ti, Y and Zr in Ascot Formation metabasalts, SE Quebec. Contrib. Mineral. Petrol. 75, 79–87.

Jahn, B.M., Wu, F.Y., Lo, C.H., Tsai, C.H., 1999. Crust–mantle interaction induced by deep subduction of the continental crust: geochemical and Sr–Nd isotopic evidence from post-collisional mafic-ultramafic intrusions of the northern Dabie complex, central China. Chem. Geol. 157, 119–146.

Jenner, G.A., 1996. Trace element geochemistry of igneous rocks: geochemical nomenclature and analytical geochemistry. In: Wyman, D.A. (Ed.), Trace Element Geochemistry of Volcanic Rocks: Applications for Massive Sulfide Exploration: Geological Association of Canada Short Course Notes, 12, pp. 51–77.

Jiang, S.Y., 2000. Controls on the mobility of high field strength elements (HFSE), U, and Th in an ancient submarine hydrothermal system of the Proterozoic Sullivan Pb–Zn–Ag deposit, British Columbia, Canada. Geochem. J. 34, 341–348.

Jiang, S.Y., Wang, R.C., Xu, X.S., Zhao, K.D., 2005. Mobility of high field strength elements (HFSE) in magmatic-, metamorphic-, and submarine-hydrothermal systems. Phys. Chem. Earth 30, 1020–1029.

Johnson, J.W., Oelkers, E.H., Helgeson, H.C., 1992. SUPCRT92: a software package for calculating the standard molal thermodynamic properties of minerals, gases, aqueous species, and reactions from 1 to 5000 bars and 0° to 1000 °C. Comput. Geosci. 18, 899–947.

Kerrich, R., Cassidy, K.F., 1994. Temporal relationships of lode gold mineralization to accretion, magmatism, metamorphism and deformation: Archean to present: a review. Ore Geol. Rev. 9, 263–310.

Küpeli, S., 2010. Trace and rare-earth element behaviors during alteration and mineralization in the Attepe iron deposits (Feke-Adana, southern Turkey). J. Geochem. Explor. 105, 51–74.

Li, Z.L., Yang, M.Z., 1993. The Geology and Geochemistry of Gold Deposits in Jiaodong Region. Tianjin Science and Technology Press, Tianjian (in Chinese).

Li, J.W., Vasconcelos, P.M., Zhang, J., Zhou, M.F., Zhang, X.J., Yang, F.H., 2004. $^{40}Ar/^{39}Ar$ constraints on a temporal link between gold mineralization, magmatism, and continental margin transtension in the Jiaodong Gold Province, Eastern China. J. Geol. 111, 741–751.

Li, J.W., Vasconcelos, P.M., Zhou, M.F., Zhao, X.F., Ma, C.Q., 2006. Geochronology of the Pengjiakuang and Rushan gold deposits, Eastern Jiaodong Gold Province, Northeastern China: implications for regional mineralization and geodynamic setting. Econ. Geol. 101, 1023–1038.

Li, S.X., Liu, C.C., An, Y.H., Wang, W.C., Huang, T.L., Yang, C.H., 2007. Ore Deposit Geology of the Jiaodong Gold Province. Geology Press, Beijing (in Chinese).

Li, X.C., Fan, H.R., Santosh, M., Hu, F.F., Yang, K.F., Lan, T.G., Liu, Y.S., Yang, Y.H., 2012. An evolving magma chamber within extending lithosphere: An integrated geochemical, isotopic and zircon U–Pb geochronological study of the Gushan granite, eastern North China Craton. J. Asian Eart Sci. 50, 27–43.

Li, S.R., Santosh, M., Zhang, H.F., Shen, J.F., Dong, G.C., Wang, J.Z., Zhang, J.Q., 2013. Inhomogenous lithospheric thinking in the central North China Craton: U–Pb and S–He–Ar isotopic record from magmatism and metallogeny in the Taihang Mountains. Gondwana Res. 21, 141–160.

Ling, H.F., Hu, S.X., Sun, J.G., Ni, P., Shen, K., 2002. Geochemical study of granitic wall-rock alteration in Dayinggehuang gold deposit of alteration rock type and Jinqingding gold deposit of quartz-vein type. Miner. Deposits 21, 187–199 (in Chinese with English abstract).

Liu, J.L., Davis, G.A., Lin, Z., Wu, F.Y., 2005. The Liaonan metamorphic core complex, Southeastern Liaoning Province, North China: a likely contributor to Cretaceous rotation of Eastern Liaoning, Korea and contiguous areas. Tectonophysics 407, 65–80.

Lu, G., Kong, Q., 1993. Geology of Linglong- and Jiaojia-style Gold Deposits in Jiaodong. Science Press, Beijing (in Chinese).

Lugmair, G.W., Harti, K., 1978. Lunar initial $^{143}Nd/^{144}Nd$: differential evolution of the lunar crust and mantle. Earth Planet. Sci. Lett. 39, 349–357.

Luo, W., Wu, Q., 1987. Timing of gold mineralization in the Jiaodong Region: constraints from isotopic dating on alteration minerals. Ore Depos. Geol. 1, 78–82 (in Chinese).

Mao, J.W., Wang, Y.T., Li, H.M., Pirajno, F., Zhang, C.Q., Wang, R.T., 2008. The relationship of mantle-derived fluids to gold metallogenesis in the Jiaodong Peninsula: evidence from D-O-C-S isotope systematics. Ore Geol. Rev. 33, 361–381.

Michard, A., 1989. Rare earth element systematics in hydrothermal fluids. Geochim. Cosmochim. Acta 53, 745–750.

Mikucki, E.J., 1998. Hydrothermal transport and depositional processes in Archean lode-gold systems: a review. Ore Geol. Rev. 13, 307–321.

Panahi, A., Young, G.M., Rainbird, R.H., 2000. Behavior of major and trace elements (including REE) during Paleoproterozoic pedogenesis and diagenetic alteration of an Archean granite near Ville Marie, Quebec, Canada. Geochim. Cosmochim. Acta 64, 2199–2220.

Phillips, G.N., Evans, K.A., 2004. Role of CO_2 in the formation of gold deposits. Nature 429, 860–863.

Plümper, O., Putnis, A., 2009. The complex hydrothermal history of granitic rocks: multiple feldspar replacement reactions under subsolidus conditions. J. Petrol. 50, 967–987.

Putnis, A., Hinrichs, R., Putnis, C.V., Golla-Schindler, U., Collins, L.G., 2007. Hematite in porous red-clouded feldspars: evidence of large-scale crustal fluid–rock interaction. Lithos 95, 10–18.

Qian, Q., Hermann, J., 2010. Formation of high-Mg diorites through assimilation of peridotite by monzodiorite magma at crustal depths. J. Petrol. 51, 1381–1416.

Qiu, Y.M., Groves, D.I., McNaughton, N.J., Wang, L.G., Zhou, T.H., 2002. Nature, age, and tectonic setting of granitoid-hosted, orogenic gold deposits of the Jiaodong Peninsula, eastern North China craton, China. Miner. Deposita 37, 283–305.
Ren, J., Tamaki, K., Li, S., Zhang, J., 2002. Late Mesozoic and Cenozoic rifting and its dynamic setting in eastern China and adjacent areas. Tectonophysics 344, 175–205.
Robert, F., Kelly, W.C., 1987. Ore-forming fluids in Archean gold-bearing quartz veins at the Sigma mine, Abitibi greenstone belt, Québec, Canada. Econ. Geol. 82, 1464–1482.
Salvi, S., Williams-Jones, A.E., 1996. The role of hydrothermal processes in concentrating high-field strength elements in the Strange Lake peralkaline complex, northeastern Canada. Geochim. Cosmochim. Acta 60, 1917–1932.
Salvi, S., Fontan, F., Monchoux, P., Williams-Jones, A.E., Moine, B., 2000. Hydrothermal mobilization of high field strength elements in alkaline igneous systems: evidence from the Tamazeght Complex (Morocco). Econ. Geol. 95, 559–576.
Schilling, J.G., 1973. Iceland Mantle Plume: geochemical study of Reykjanes ridge. Nature 242, 565–571.
Scholz, C.H., 1988. The brittle-plastic transition and the depth of seismic faulting. Geol. Rundsch. 77, 319–328.
Seward, T.M., 1973. Thio complexes of gold and the transport of gold in hydrothermal ore solutions. Geochim. Cosmochim. Acta 37, 379–399.
Sibson, R.H., 1977. Fault rocks and fault mechanisms. J. Geol. Soc. 33, 191–213.
Stefánsson, A., Seward, T.M., 2004. Gold(I) complexing in aqueous sulphide solutions to 500 °C at 500 bar. Geochim. Cosmochim. Acta 68, 4121–4143.
Sun, S.S., McDonough, W.F., 1989. Chemical and isotopic systematics of oceanic basalts: implications for mantle composition and processes. In: Saunders, A.D., Norry, M.J. (Eds.), Magmatism in the Oceanic Basalts: Geological Society Special Publication, pp. 313–345.
Sverjensky, D.A., Hemley, J.J., D'Angelo, W.M., 1991. Thermodynamic assessment of hydrothermal alkali feldspar–mica–aluminosilicate equilibria. Geochim. Cosmochim. Acta 55, 989–1004.
Tam, P.K., Zhao, G.C., Liu, F., Zhou, X., Sun, M., Li, S.Z., 2011. Timing of metamorphism in the Paleoproterozoic Jiao-Liao-Ji Belt: New SHRIMP U–Pb zircon dating of granulites, gneisses and marbles of the Jiaobei massif in the North China Craton. Gondwana Res. 19, 150–162.
Tang, J., Zheng, Y.F., Wu, Y.B., Gong, B., Liu, X.M., 2007. Geochronology and geochemistry of metamorphic rocks in the Jiaobei terrane: constraints on its tectonic affinity in the Sulu orogen. Precambrian Res. 152, 48–82.
Tian, Z.Y., Han, P., Xu, K.D., 1992. The Mesozoic–Cenozoic East China rift system. Tectonophysics 208, 341–363.
Wang, L.G., Qiu, Y.M., McNaughton, N.J., Groves, D.I., Luo, Z.K., Huang, J.Z., 1998. Constraints on crustal evolution and gold metallogeny in the northwestern Jiaodong Peninsula, China, from SHRIMP U–Pb zircon studies of granitoids. Ore Geol. Rev. 13, 275–291.
White, J.C., 2003. Trace-element partitioning between alkali feldspar and peralkalic quartz trachyte to rhyolite magma. Part II: empirical equations for calculating trace-element partition coefficients of large-ion lithophile, high field-strength, and rare-earth elements. Am. Mineral. 88, 330–337.
Williams-Jones, A.E., Bowell, R.J., Migdisov, A.A., 2009. Gold in solution. Elements 5, 281–287.
Xu, Y.G., Huang, X.L., Ma, J.L., Wang, Y.B., Iizuka, Y., Xu, J.F., Wang, Q., Wu, X.Y., 2004. Crust–mantle interaction during the tectono-thermal reactivation of the North China Craton: constraints from SHRIMP zircon U–Pb chronology and geochemistry of Mesozoic plutons from western Shandong. Contrib. Mineral. Petrol. 147, 750–767.
Yang, J.H., 2000. Age and metallogenic dynamics of gold mineralization in Jiaodong Peninsula, eastern China—constraints on the interaction of mantle/crust and metallogenesis/lithospheric evolution. [Ph.D. thesis]: Beijing, Institute of Geology and Geophysics, Chinese Academy of Sciences, 133 pp (in Chinese with English abstract).
Yang, M.Z., Lu, G.X., 1996. The Geology–Geochemistry of Gold Deposits of the Greenstone Belt in the Jiaodong District. Geological Publishing House, Beijing (in Chinese).
Yang, J.H., Zhou, X.H., 2001. Rb–Sr, Sm–Nd, and Pb isotope systematics of pyrite: implications for the age and genesis of lode gold deposits. Geology 29, 711–714.
Yang, Z.F., Xu, J.K., Zhao, L.S., Shen, Y.L., Wu, Y.B., 1998. The Evolution of Regional Crust and the Geochemistry on Gold Mineralization in Jiaodong. Geological Publishing House, Beijing (in Chinese with English abstract).
Yang, J.H., Chung, S.L., Zhai, M.G., Zhou, X.H., 2004. Geochemical and Sr–Nd–Pb isotopic compositions of mafic dikes from the Jiaodong Peninsula, China: evidence for vein-plus-peridotite melting in the lithospheric mantle. Lithos 73, 145–160.
Yang, K.F., Fan, H.R., Santosh, M., Hu, F.F., Wilde, S.A., Lan, T.G., Lu, L.N., Liu, Y.S., 2012. Reactivation of the Archean lower crust: implications for zircon geochronology, elemental and Sr–Nd–Hf isotopic geochemistry of late Mesozoic granitoids from northwestern Jiaodong Terrane, the North China Craton. Lithos 146–147, 112–127.
Yardley, B.W.D., 2005. Metal concentrations in crustal fluids and their relationship to ore formation. Econ. Geol. 100, 613–632.
Zhai, M.G., 2008. Lower crust and lithospheric mantle beneath the North China Craton before the Mesozoic lithospheric disruption. Acta Petrol. Sin. 24, 2185–2204 (in Chinese with English abstract).
Zhai, M.G., Santosh, M., 2011. The Early Precambrian odyssey of the North China Craton: a synoptic overview. Gondwana Res. 20, 6–25.
Zhai, M.G., Fan, H.R., Yang, J.H., Miao, L.C., 2004. Large-scale cluster of gold deposits in east Shandong: anorogenic metallogenesis. Earth Sci. Front. 11, 85–98 (in Chinese with English abstract).
Zhang, X.O., Cawood, P.A., Wilde, S.A., Liu, R.Q., Song, H.L., Li, W., Snee, L.W., 2003. Geology and timing of mineralization at the Cangshang gold deposit, north-western Jiaodong Peninsula, China. Miner. Deposita 38, 141–153.
Zhang, L.C., Zhou, X.H., Ding, S.J., 2008. Mantle-derived fluids involved in large-scale gold mineralization, Jiaodong District, China: constraints provided by the He–Ar and H–O isotopic systems. Int. Geol. Rev. 50, 472–482.
Zhang, J., Zhao, Z.F., Zheng, Y.F., Dai, M.N., 2010. Postcollisional magmatism: geochemical constraints on the petrogenesis of Mesozoic granitoids in the Sulu orogen, China. Lithos 119, 512–536.
Zhang, H.F., Zhu, R.X., Santosh, M., Ying, J.F., Su, B.X., Hu, Y., 2013. Episodic widespread magma underplating beneath the North China Craton in the Phanerozoic: implications for craton destruction. Gondwana Res. 23, 95–107.
Zhao, G.C., Wilde, S.A., Cawood, P.A., Sun, M., 2001. Archean blocks and their boundaries in the North China Craton: lithological, geochemical, structural and P–T path constraints and tectonic evolution. Precambrian Res. 107, 45–73.
Zhao, G.C., Sun, M., Wilde, S.A., Li, S.Z., 2005. Late Archean to Paleoproterozoic evolution of the North China Craton: key issues revisited. Precambrian Res. 136, 177–202.
Zhao, Z.F., Zheng, Y.F., Chen, R.X., Xia, Q.X., Wu, Y.B., 2007. Element mobility in mafic and felsic ultrahigh-pressure metamorphic rocks during continental collision. Geochim. Cosmochim. Acta 71, 5244–5266.
Zheng, Y.F., Chen, R.X., Zhao, Z.F., 2009. Chemical geodynamics of continental subduction-zone metamorphism: insights from studies of the Chinese Continental Scientific Drilling (CCSD) core samples. Tectonophysics 475, 327–358.
Zhu, G., Song, C.Z., Wang, D.X., Liu, G.S., Xu, J.W., 2001. Studies on $^{40}Ar/^{39}Ar$ thermochronology of strike-slip time of the Tan–Lu fault zone and their tectonic implications. Sci. China Earth Sci. 44, 1002–1009.